Refining Reaction Mechanisms to Enhance Combustion Efficiency in Scramjet Propulsion Systems

a project presented to
The Faculty of the Department of Aerospace Engineering
San José State University

in partial fulfillment of the requirements for the degree
Master of Science in Aerospace Engineering

by

Alicia S. Palmerin Jimenez

December 2025

approved by

Dr. Yawo Ezunkpe
Faculty Advisor

San José State
UNIVERSITY

ABSTRACT

Refining Reaction Mechanisms to Enhance Combustion Efficiency in Scramjet Propulsion Systems

Alicia S. Palmerin Jimenez

The purpose of this project is to extend the understanding of the combustion process in a supersonic combustion ramjet (scramjet) by analyzing the effect of reaction mechanisms considered in computational fluid dynamics (CFD) simulations. Furthermore, this project demonstrates the difficulty that engineers must overcome when setting up the CFD simulation to replicate the working environment of a scramjet, and the complex theory that must be considered. The project validated the CIAM/NASA scramjet geometry by running cold flow CFD simulations, in ANSYS Fluent, against literature and theory. The project begins to analyze the flow and species characteristics when considering transient supersonic compressible flow with four reactions in the reaction mechanism for the CIAM/NASA scramjet combustion chamber with two fuel injectors.

ACKNOWLEDGEMENTS

To Professor Yawo Ezunkpe, who had complete faith in me to complete this project, despite all the trials and tribulations I had to face. I will forever be thankful for his support and motivating and encouraging words. It is because of him that I know I will accomplish all I have planned, and I hope the students to come are able to be blessed by his guidance as well.

To my hardworking parents, Hermelinda and Jesus Palmerin, who have sacrificed so much to grant me the opportunity to accomplish another milestone. I appreciate all you have done for me, and I hope to continue to make you proud. This degree is for you.

To my brothers, Jose and Dominic Palmerin, who were always there to cheer me on and make me laugh during times I needed it most. You two gave me the motivation to continue because you never lost faith in me even when I was losing faith in myself.

To my friends and family, who were always willing to listen to me complain about how stressed I was. Your companionship and willingness to do whatever you could to help lessen the weight I had on my shoulders will forever be remembered. I am eternally grateful for you and am blessed to have lovely people as yourselves in my life.

To my significant other, Rudy Moreno, who believed in me every step of the way and encouraged me to push through no matter the obstacles I had to face. Thank you for bearing with me through sleepless nights and hearing me talk about my research at random times. I am blessed to have such a supportive partner as yourself.

To my dog, Apollo, who was literally by my side each time I pulled an all-nighter. My constant companion through it all. You showed me what it is like to handle many things at once. Here's to all the dog treats I will buy you one day.

Table Of Contents

Abstract iii
Acknowledgements iv
Table Of Contents v
List of Figures vii
List of Tables viii
Symbols ix
1. Introduction 12
- 1.1 Motivation 12
- 1.2 Literature Review 12
  - 1.2.1 Scramjet Propulsion System 12
  - 1.2.2 Fuel Considerations 15
  - 1.2.3 Challenges 16
  - 1.2.4 Advancements 17
- 1.3 Project Proposal 18
- 1.4 Methodology 18

2. Scramjet Design and Function 19
- 2.1 Scramjet Historical Overview 19
- 2.2 Scramjet Design 22
  - 2.2.1 Inlet 22
  - 2.2.2 Isolator 26
  - 2.2.3 Combustion Chamber 27
  - 2.2.4 Exhaust Nozzle 31
- 2.3 Scramjet Geometry 32
  - 2.3.1 CIAM/NASA Scramjet Configuration 32
  - 2.3.2 CIAM/NASA Scramjet CAD 34

3. Scramjet CFD Verification 35
- 3.1 Preprocessing and Mesh Generation 35
  - 3.1.1 Geometry Preparation and Import 35
  - 3.1.2 Meshing 36
- 3.2 Boundary Conditions and Simulation Set Up 38
  - 3.2.1 General Task Page 38
  - 3.2.2 Model Selection 38
  - 3.2.3 Material Selection 38
  - 3.2.4 Boundary Conditions 38
  - 3.2.5 Wall and Outlet Conditions 39
  - 3.2.6 Reference Values 39
  - 3.2.7 Monitor Settings 39

3.2.8 Initialization..39
3.2.9 Running Calculation..39
3.3 Computational Fluid Dynamics Fundamentals..40
3.3.1 Conservation Equations..40
3.3.2 Turbulence Model..42
3.4 Results and Comparison..44
4. Scramjet Theoretical Verification..47
4.1 Oblique Shockwaves..47
4.2 Scramjet Wave Analysis and Comparison..50
5. Fuel Injection Integration..56
5.1 CAD Modifications for Fuel Injectors..56
5.2 Combustion Chamber Boundary Conditions..58
5.3 Fuel Injector Boundary Conditions..59
5.4 Updated Mesh..59
5.5 Updated Simulation Set Up..60
5.5.1 General Task Page..60
5.5.2 Model Selection..61
5.5.3 Material Selection..61
5.5.4 Cell Zone and Boundary Conditions..61
5.5.5 Wall and Outlet Conditions..62
5.5.6 Reference Values..62
5.5.7 Control and Monitor Settings..63
5.5.8 Initialization..63
5.5.9 Running Calculation..63
6. Preliminary Results..65
7. Conclusion and Future Work..71
References..75

List of Figures

Figure 1.1 - Scramjet design layout 13
Figure 1.2 - T-s Diagram for ramjets and scramjets 14
Figure 1.3 - Specific impulse as a function of mach number 15
Figure 2.1 - Scramjet inlet placement 21
Figure 2.2 - Different inlet compressions 23
Figure 2.3 - Inlet design for scramjet 24
Figure 2.4 - Inlet ramp configuration 25
Figure 2.5 - Shock and shock trains as a function mach number 27
Figure 2.6 - Back step fuel injection for scramjet 30
Figure 2.7 - Strut fuel injection for scramjet 30
Figure 2.8 - Exhaust nozzle location 31
Figure 2.9 - Simple expansion ramp nozzle design 32
Figure 2.10 - CIAM/NASA scramjet inlet geometry 33
Figure 2.11 - CIAM/NASA scramjet isolator and combustion chamber design 34
Figure 2.12 - CIAM/NASA axisymmetric dual-mode scramjet CAD 34
Figure 3.1 - Adjusted CIAM/NASA scramjet CAD 35
Figure 3.2 - CIAM/NASA scramjet mesh 36
Figure 3.3 - Face and edge sizing mesh 37
Figure 3.4 - Laminar-Turbulent flow transition 42
Figure 3.5 - Statistical decomposition of velocity component 43
Figure 3.6 - Static pressure contour 44
Figure 3.7 - Static temperature contour 45
Figure 3.8 - Mach number contour 45
Figure 4.1 - Oblique shock wave properties 47
Figure 4.2 - Oblique shock wave properties and geometry 48
Figure 4.3 - Temperature ratio as a function of mach number for inlet exit 54
Figure 4.4 - Temperature ratio as a function of mach number for inlet entrance 54
Figure 5.1 - Fuel injector dimensions at station 2 56
Figure 5.2 - Fuel injector dimensions at station 3 57
Figure 5.3 - Combustion chamber geometry with fuel injectors 57
Figure 5.4 - Combustion chamber surface 57
Figure 5.5 - Combustion Chamber Mesh 60
Figure 6.1 - Static pressure contour as a result of fuel injection 65
Figure 6.2 - Static temperature contour after fuel injection 66
Figure 6.3 - Mass fraction of oxygen after fuel injection 67
Figure 6.4 - Mass fraction of liquid hydrogen after fuel injection 68
Figure 6.5 - Mass fraction of water vapor after fuel injection 69
Figure 6.6 - Heat of reaction after fuel injection 70

List of Tables

Table 3.1 - General Mesh Information	37
Table 4.1 - First Oblique Shock Wave	51
Table 4.2 - Second Oblique Shock Wave	52
Table 4.3 - Third Oblique Shock Wave	53
Table 5.1 - Combustion Chamber Entrance Conditions	58
Table 5.2 - Fuel Injector Conditions	59
Table 5.3 - Combustion Chamber Mesh Information	60
Table 5.4 - Fuel Injector Direction	62

Symbols

Symbol	Definition	Units (SI)
M	Mach Number	unitless
T	Temperature	K
s	Entropy	J/K
P	Pressure	Pa
ρ	Density	kg/m^3
w	Z-component of Velocity	m/s
v	Y-component of Velocity	m/s
U	Velocity Magnitude	m/s
h	Enthalpy	J
u	X-Component of Velocity	m/s
V	Velocity Vector	m/s
e	Internal Energy	J
$\dot{W}$	Rate of Work	W
F	Viscous Force Vector	N
$\dot{q}$	Heat Flow Rate	W
f	Net Body Force Vector	N
x	X-coordinate in Space	unitless
y	Y-coordinate in Space	unitless
z	Z-coordinate in Space	unitless
Re	Reynolds Number	unitless
Pr	Prandtl Number	unitless
q	Heat Flux	W/m^2
S	Heat of Chemical Reaction	kJ/mol
J	Diffusion Flux	mol/m^2s
L	Length	m
E	Energy	J
k	Thermal Conductivity	W/m·K
t	Time	s
V'	Fluctuation Velocity Vector	m/s
$\overline{\mathbf{V}}$	Mean Velocity Vector	m/s
k	Turbulent Kinetic Energy	J/kg
D	Cross-Diffusion Term	m^2/s
S	User-Defined Terms	
Y	Turbulent Dissipation Rate Generated	m^2/s^3
G	Specific Dissipation Rate Generation	1/s
N	Number of Time Steps	unitless
G_k	Turbulent Kinetic Energy Generated by Mean Velocity Gradient	J/kg

Greek Symbols		
η	Combustion Efficiency	%
π	Combustion Total Pressure Ratio	unitless
β	Wave Angle	Degrees
μ	Viscosity	Pa·s
τ	Stress Tensor	Pa
τ	Turbulence Intensity	unitless
θ	Deflection Angle	Degrees
ω	Specific Dissipation Rate	1/s
Γ	Effective Diffusivity	m^2/s
Subscripts		
$()_b$	Burner	
$()_0$	Stagnation	
$()_T$	Turbulent	
$()_L$	Laminar	
$()_1$	Upstream First Shockwave	
$()_2$	Downstream First Shockwave	
$()_3$	Downstream Second Shockwave	
$()_4$	Downstream Third Shockwave	
$()_n$	Normal Component	
$()_{xx}$	X-X Component of 3D Tensor	
$()_{xy}$	X-Y Component of 3D Tensor	
$()_{xz}$	X-Z Component of 3D Tensor	
$()_{yy}$	Y-Y Component of 3D Tensor	
$()_{yz}$	Y-Z Component of 3D Tensor	
$()_{zz}$	Z-Z Component of 3D Tensor	
$()_t$	Total	
$()_j$	Species	
$()_i$	Species	
$()_{eff}$	Effective	
Acronyms		
SERN	Single Expansion Ramp Nozzle	
CIAM	Central Institute of Aviation Motors	

NASA	National Aeronautics and Space Administration	
CAD	Computer-aid Design	
CFD	Computational Fluid Dynamics	
PDEs	Partial Differential Equations	
TBCC	Turbine Based Combined Cycle	
RBCC	Rocket Based Combined Cycle	
SSTO	Single-stage-to-orbit	
TSTO	Two-stage-to-orbit	
ER	Equivalence Ratio	
AI	Artificial Intelligence	
DRCN	Lightweight Deformable Convolutional Residual Neural Network	
NASP	National Aerospace Plane	
SCRAM	Supersonic Combustion Ramjet	
HRE	Hypersonic Research Engine	
APL	Applied Physics Laboratory	
CFL	Courant-Friedrichs-Lewy number	

1. Introduction

1.1 Motivation

The pursuit of unprecedented speeds remains a fundamental objective for engineers. This is particularly true as technological advancements continue to transform this once distant aspiration into a tangible, achievable reality. Ever since the mere idea came into existence in the 1960's, supersonic combustion ramjets, scramjets, have been at the forefront of hypersonic propulsion, despite there being one major problem. The challenge in achieving efficient and stable combustion at hypersonic speeds is hindering the practical application of scramjets. The working fluid, air, for a scramjet is traveling more than three times the speed of sound, which results in issues with having sufficient time to combust the entirety of the fuel and air while ensuring the structure can tolerate the extreme temperatures and pressures. Once the complexities of scramjets have been understood, scramjets will revolutionize the military, public transport, and space travel sectors. In the military and defense sector, scramjets will allow for missiles to reach hypersonic speeds, thus having the ability to eliminate any threats in record time. Northrop Grumman, one of the leading defense companies in the aerospace field, have acknowledged the importance of having hypersonic missiles by means of a scramjet as the main objectives in the defense are stealth and speed [1]. In the passenger aircraft sector, Concorde left the engineering world with plenty of thoughts about what could have been done better. Hermes, a startup based in Atlanta, Georgia, may have found an alternative as they plan to develop a passenger aircraft that will utilize a scramjet to travel up to Mach 5 [2]. Not only does it further decrease the time to travel from New York to London, but it is a more efficient and cleaner method, if hydrogen is chosen as fuel. Further exciting the possibilities scramjets will bring. Finally, in the space travel sector, pairing a scramjet with a rocket can reduce costs and complexity of reaching orbit, instead of having a multi-stage heavy rocket. The pairing will be especially beneficial for reusable launch vehicle purposes. NASA's X-43A is proof that having a scramjet will allow the launch vehicle to get the altitude needed, as the X-43A reached an altitude of 110,000 feet at Mach 9.5 [3]. The versatility of scramjets positions them as a key technology in shaping the future of both aerospace and defense industries. The research conducted in this master's project aims to address complexities associated with scramjet technology, seeking to enhance its understanding and contribute to the development of more efficient propulsion systems.

1.2 Literature Review

1.2.1 Scramjet Propulsion System

A ramjet operates by taking in supersonic air, specifically Mach 1-3, and decelerating it to subsonic speeds before it enters the combustor, where it is then injected with fuel at a subsonic rate. The result of the mixture, being hot gas, is then expelled through a nozzle for thrust [4,5]. However, as the velocity of the air increases substantially, ramjets become inefficient due to extreme pressures and temperatures and having to inject fuel at faster rates. To combat this issue, supersonic combustion ramjets (scramjets) are utilized, capable of operating efficiently at Mach 4-7 [6]. The design of a scramjet is displayed in **Figure 1.1**, but the overall components are: the inlet, the isolator, the combustor, and the nozzle. Both ramjets and scramjets have a converging-diverging nozzle design. However, the scramjet engine isn't enough to provide thrust for liftoff, it needs the assistance of a propulsion vehicle, i.e. another air breathing engine, to reach those supersonic speeds [7].

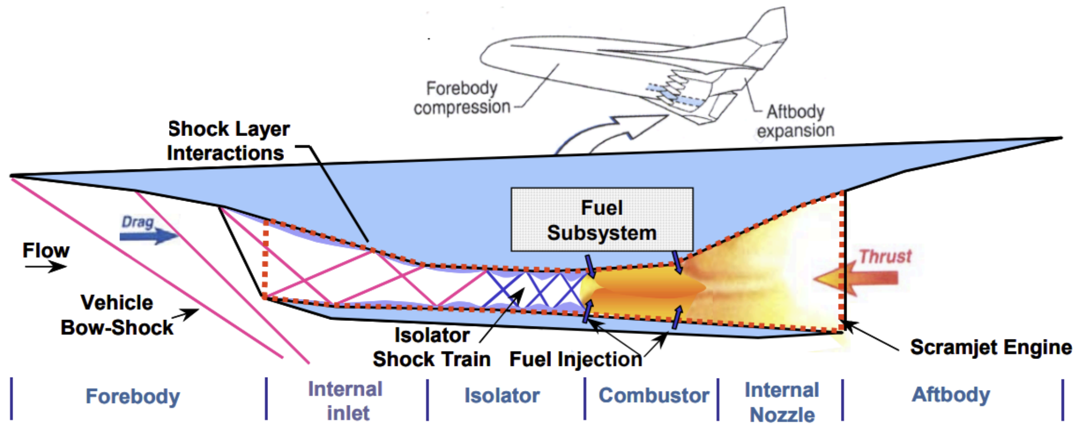

Figure 1.1 - Scramjet design layout [8]

The compression of air begins at the forebody of the vehicle, as seen in **Figure 1.1**. The geometry of the forebody also assists with creating shock waves, where the majority are oblique shock waves, that will continue throughout the inlet and isolator, further compressing the air as it prepares to mix with the fuel [7]. As mentioned before, the fuel has to be injected at supersonic speeds. As the fuel is mixing with the incoming compressed air within microseconds, it is important to ensure mixing control takes precedence [9]. The rate at which the air mixes with the fuel affects the combustion rate, i.e. better mixing results in a better combustion rate [10]. Ideally, the combustion process should be able to have complete mixing, ignite all of the air/fuel mixture rather quickly, and generate the maximum amount of heat possible while keeping pressure loss to a minimum [9]. With minimal pressure loss, there will be a larger pressure difference between the resultant pressure from the combustion process and the ambient pressure, resulting in maximum thrust [7].

In addition to requiring another air-breathing engine to reach supersonic speeds that will allow the scramjet to function effectively, it also relies on a high-performance Brayton cycle. The Brayton cycle can be described in a T-s diagram as seen in **Figure 1.2**.

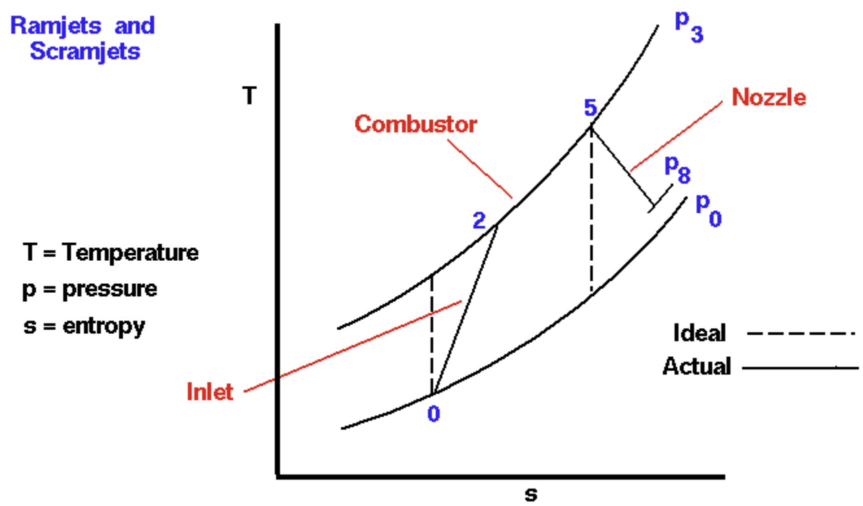

Figure 1.2 - T-s Diagram for ramjets and scramjets [11]

Between point 0 and point 2, there is ideally isentropic compression, where inlet geometry increases air pressure and temperature for fuel mixing [12]. Realistically, there is non-isentropic compression at the inlet due to energy losses, which increase the entropy of the system [11]. From point 2 to point 5, there is constant-pressure heat addition to the system, where heat is released in a constant-area and diverging combustion chamber [12]. The exact increase in temperature is a function of the type of fuel chosen and the fuel to air ratio [11]. From point 5 to point 8, there is ideally isentropic expansion, where airflow expands through the nozzle for optimized performance. As with the compression, there is the possibility of losses due to friction and viscous dissipation, leading to an entropy increase [13]. Not depicted in Fig. 1.2 is a path between point 8 and point 0, there is constant-pressure heat rejection, representing the difference between nozzle exit and free-stream conditions [12].

Considering only a scramjet, the thermodynamic cycle mentioned above would well enough assist engineers in optimizing its performance. Yet, as the vehicle requires another engine in order for the scramjet to operate, there will now be combined thermodynamic cycles that will allow for overall optimization [13]. The first cycle being the Turbine Based Combined Cycle, or TBCC. It consists of using a turbojet, or turbofan, to reach the supersonic speeds needed for a ramjet, or scramjet [13]. As the aircraft's speed exceeds Mach 3, the afterburner then functions as a ramjet, or scramjet. The turbojet's maximum temperature has to decrease in order to prevent any damage to rotating parts, while ensuring that the flow can pass through to the afterburner and increase the thrust. Aircraft that have used a TBCC include the SR-71 Blackbird and NASA's X-43. The second cycle is the Rocket Based Combined Cycle, or RBCC. As the name entails, it consists of a rocket and either a ramjet or scramjet. Depending on the mission objectives, either engine or rocket or a combination of each can be utilized to reach the desired destination. If considering the latter option, the rocket is used as an ejector, where the exhaust plume is serving as the main flow for either the ramjet, or scramjet, and the incoming air is the second flow. By having two sources of flow, the overall mass flow the engine receives. In return, there is a larger amount of thrust generated. RBCC in a rocket-ejector scramjet is ideal for single-stage-to-orbit (SSTO) or two-stage-to-orbit (TSTO) spacecraft [13,14].

1.2.2 Fuel Considerations

There are plenty of parameters of a scramjet that can be adjusted to ensure it can function at its full capacity. However, the choice of fuel is one of the most important parameters to consider, especially since it is more feasible to analyze its effects on thrust through numerical simulation. The lower heating value of the fuel greatly affects how it mixes with the working fluid and ignites in the combustion chamber. The lower heating value refers to the amount of heat released when a certain amount of fuel, in this case, is combusted. It is desired to pick a fuel that has a higher lower heating value, as it will produce more energy and thus more thrust. For instance, Roberts [15] concluded that the freestream Mach number cannot be lowered to Mach 3.5 due to the lower heating value of the chosen fuel, JP-7. JP-7 has a smaller lower heating value compared to the popular choice, hydrogen. Over the years, hydrogen has been the leading selection for fuel as it has the highest lower heating value and is considered a clean gas as it produces water vapor. In addition, it also offers a higher specific impulse compared to other fuels, such as hydrocarbons. **Figure 1.3** displays the difference in specific impulse for both hydrogen and hydrocarbon as fuel choice.

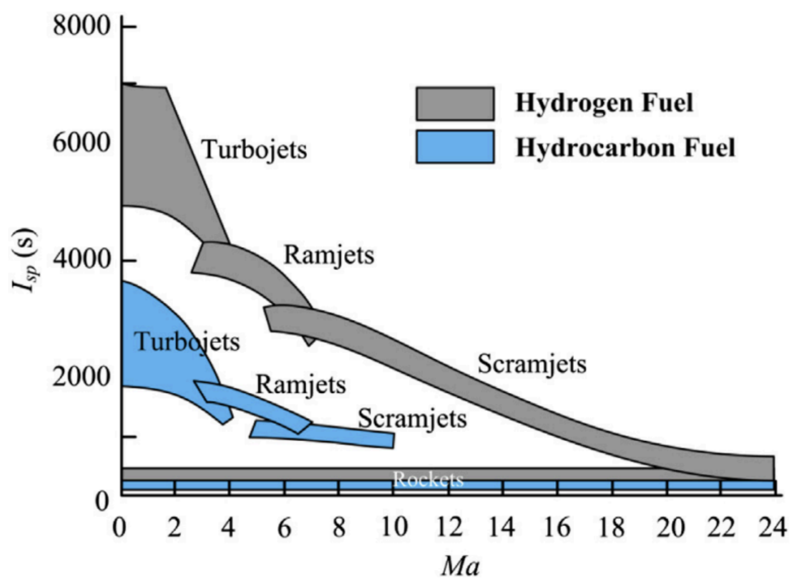

Figure 1.3 - Specific impulse as a function of mach number [16]

From **Figure 1.3**, utilizing hydrogen as fuel will result in a considerable increase in specific impulse compared to utilizing hydrocarbons as fuel. Furthermore, hydrogen offers a larger range for freestream Mach number, which is desirable considering achieving hypersonic speeds is the overall goal of a scramjet.

While **Figure 1.3** displays that hydrogen is the more beneficial fuel choice, thought must be given to the reaction mechanism that will be utilized for numerical analysis. The process when the fuel mixes with the incoming flow is not instantaneous, there is a sequence of elementary reactions occurring that will eventually lead to the final product. The more detailed, i.e. the more sequences considered, the more accurate the analysis as it is more representative of the actual process occurring in the combustion chamber. For example, the reaction mechanism E.

Distaso et al. [17] utilized 10 species and 21 steps, whereas Engman's [18] consisted of 13 species and 33 steps. Ultimately, the amount of species/steps desired is dependent on the computational power available.

Another parameter that assists in determining the efficiency of the combustion process is the equivalence ratio (ER) for the given fuel choice. All studies mentioned will have used hydrogen gas as the fuel. The equivalence ratio describes the ratio of fuel to oxidizer, the incoming air in the case of a scramjet, to its stoichiometric value. G. Ma et al. [6] found that increasing the ER from 0.2 to 0.5 to 0.8 resulted in an increase in maximum thrust produced. A consequence of the increase in thrust as the ER increased was that more compression would be required to meet said maximum thrust. [6] states that a possible reason for needing more compression is flow loss due to heat release. Similarly, Y. Tien et al. [19] found that as the ER increased from 0.1 to 0.3, the hydrogen took longer to ignite. For an ER of 0.1, it took approximately 0.010 seconds to ignite, whereas for an ER of 0.3, it took 0.022 seconds. This is an important distinction since there is an extremely short time given in the combustion process to have as much of the fuel/air mixture to burn. Interestingly, when the diffusion process in the combustion chamber is replaced with oblique shock waves and/or detonation waves, the ER does not have such a large effect on one efficiency parameter, combustion pressure. K. Ma et al. [20] found that for a shock-induced combustion ramjet (shcramjet) increasing the ER from 0.5 to 1.0 had minimal effect on the pressure ratio even at two different temperatures, 1000 K and 1500 K. Besides the pressure ratio, [20] states that if the flow is to be steady, decreasing the ER will ensure that the C-J (Chapman-Jouguet) detonation velocity decreases, and thus stability is achieved.

1.2.3 Challenges

Scramjets represent a crucial advancement in propulsion technology for hypersonic flight, offering the potential to revolutionize space access, military operations, and atmospheric flight at extreme speeds. The simplicity of their design makes them an ideal propulsion candidate as it excludes any moving parts and does not require any oxidizer to be on board, reducing the overall mass and cost of the engine. Even so, the simplicity of the scramjet is not without its drawbacks.

One challenge is ensuring that there is the right amount of compression at the inlet and isolator in order to produce the maximum amount of thrust when traveling at a high Mach number. G. Ma et al. [6] modified the thermodynamic cycle and utilized five different scramjet designs in order to conduct theoretical and numerical analysis regarding efficiency parameters of a scramjet traveling at Mach 8 and Mach 10. [6] concluded that flow loss is a result of excessive compression and a weak combustion efficiency is a result of insufficient compression. Sufficient compression can be obtained by compressing the flow at the inlet to Mach 4 and Mach 5, respectively, to ensure that maximum thrust is achieved. While the study focuses on only two Mach numbers, it demonstrates the consideration that is needed when designing a scramjet if speeds higher than those mentioned are desired.

As the Mach number increases, a scramjet has to further compress the incoming air. As a result, and assuming there is minimal pressure loss, the pressure will significantly increase and thus, the temperature will as well. The material of the scramjet has to be strong enough to endure the extreme temperature inside. In addition, if the scramjet is going to be paired with a rocket for space travel, the material will also have to withstand the aerodynamic heating. The selection of material will also have to consider weight, as one of the goals is for the scramjet to be lightweight.

While there are plenty of challenges regarding the development of scramjets, the most pressing issue is the complexity of the aero-thermo-chemistry aspect. Aforementioned, a complete combustion process consists of the injecting the fuel, allowing it to mix with the incoming air, ignite, and combust all within microseconds. The task itself may be difficult, but understanding it and attempting to duplicate the process in numerical simulations or experiments is labrouts. K. Ma et al. [20] specifies the lack of theories for the propulsive performance on a scramjet that considers one-dimensional, steady-state, heat-addition flow. The authors state that there is one theory that has been utilized even up until today's age, yet it proves to be minimally accurate when considering the more realistic-unpredictable phenomena, like shock-shock interactions, occurring in the combustion chamber. Distaso et al. [17] further supports [20] by mentioning that the difficult unsteady phenomena to model includes flow turbulence, miniscule spatial scales, and shock-boundary layer interactions. To attempt and analyze everything mentioned above, capable computational power is required. Technology may be advancing and there may be adequate programs and supercomputers, does not necessarily imply that the realistic, complex flow in a scramjet will be easier to model and analyze. Assumptions are needed to ease the computational time, which only gives a brief understanding of the aero-thermo-chemistry aspect. In addition, it would be safe to assume that if numerical simulations are not possible, then experiments must be. Unfortunately, conducting physical experiments are even more difficult as they require a proper testing site and are quite expensive. It takes high-level equipment to be able to study the flow in a physical scramjet.

1.2.4 Advancements

As previously stated, advancements in technology have significantly contributed to the progress of various aspects in scramjet technology. For instance, Artificial Intelligence (AI) has become a common method of analysis as significant improvements have been made to computing power. In addition to making assumptions to simplify the computing time, narrowing in the focus is also beneficial. Various attempts to understand the complex combustion chamber flow field through different iterations of neural networks and deep learning methods have been made since 2016. The goal for most research, using said methods, is to be able to predict the evolution of flame propagation, as the efficiency of combustion is dependent on the flame. Deng et al. [21] utilized a Lightweight Deformable Convolutional Residual Neural Network (DRCN) to use wind tunnel data for a scramjet at Mach 2.5, specifically combustion chamber wall pressure data, as input in order to predict the behavior of the flame field at different time interval. [21] mentioned that with using a deformable convolutional layer, the intricate details of the flame shape and its behavior with time can be accurately captured. The more accurate the flame can be studied, the more accurate the generalizations can be regarding the prediction of flame as time evolves. The authors found that the DRCN met the expectations as it provided a better signal-to-noise ratio and image quality, while the results consisted of only 1.24 MB of data. It may not answer all the questions about the aero-thermo-chemistry aspect of scramjet combustion, but it does serve as another efficient methodology to focus on further understanding a smaller aspect, such as flame characteristics [21].

Hydrogen may be the fuel of choice considering its high lower heating value and high specific impulse, as seen in Fig. 3. However, there have also been recent developments in the selection of fuel for scramjets. Boron has been of interest as it has a high volumetric and gravimetric energy potential, making it a valuable metal to be added to hydrocarbons [22]. To have the benefits of both liquid and solid fuels, gel-fuels are considered. Specifically, boron-loaded gel fuels. Madhumitha et al. [22] conduct a review regarding boron-loaded gel fuels in application for scramjets as the literature is scarce. [22] mentions that a study was done comparing the effects of using JP-10 gel fuel and boron-loaded JP-10 gel fuel. It was found that the latter 3.5% increase in combustion efficiency, a 8.42% increase in specific impulse, and a higher heat flux temperature. While the results are rather impressive, further studies must be conducted in order to generalize that boron-loaded gel fuels can be a potential fuel choice. It is a result of the nature of boron, where it requires two-stage combustion to burn fully [22]. Investing effort into the effects of boron-loaded gel fuels will potentially increase the selection of fuels, beneficial for specific needs by stakeholders.

While these advancements have significantly contributed to the development of scramjets, further research and innovation are still required to fully harness their potential. As the understanding of scramjet technology continues to evolve, it is foreseeable that scramjets could play a pivotal role in the development of reusable launch vehicles. **Figure 1.3** demonstrates that scramjets have a higher specific impulse compared to rockets. Nevertheless, it was mentioned before that scramjets need another propulsive device in order to reach operating speeds. If a rocket based combined cycle (RBCC) is considered, then the mission can still obtain the benefits of a scramjet, such as less weight and higher propulsion efficiency. Furthermore, a RBCC will improve the technological aspect of the mission, but also revolutionize space access with more cost-effective and efficient solutions [23].

1.3 Project Proposal

The objective of this master's project is to study the effect of different reaction mechanisms for hydrogen on the performance and efficiency of the combustion process in a scramjet. The reaction mechanism for an advanced fuel, boron-loaded gel fuels, will also be considered. The focus will be to determine if the number of species and sequences considered for the reaction mechanism for hydrogen have significant impacts on parameters such as fuel concentration, fuel-to-air ratio, equivalence ratio, combustion chamber wall pressure, heat release rate, thermal efficiency. It will then be compared to the resultant parameters of utilizing the boron-loaded gel fuel to determine which fuel is more beneficial for a scramjet. The overall goal is to optimize the combustion process for a scramjet, by ensuring a majority of the fuel-air mixture burns with the allotted time and produces a significant pressure difference, with minimal pressure loss.

1.4 Methodology

Accomplishing the goal of optimizing scramjet performance via reaction methods is multifaceted. The first step is to use CAD to design the overall scramjet: inlet, isolator, combustor, and nozzle included. Literature will be referenced to certify that the design is well within reason. This step is to guarantee that the optimization considers the overall scramjet performance and demonstrate how the components interact to produce the parameters of interest. Once the design of the scramjet has completed, detailed reaction mechanisms from literature will be implemented into computational fluid dynamics (CFD) analysis. Regarding CFD, the mathematical foundations for chemical kinetics, transport phenomena, thermochemistry, and turbulent flow must be understood in order to truly understand the analysis process, as well as the results obtained. Moreover, the theories surrounding turbulent flow must also be studied. Reynolds-Averaged Navier-Stokes models and Large Eddy Simulations are the most common theories used in CFD. Once results have been obtained, they will be compared to existing literature to confirm that they are within a reasonable range. They will also be compared against each other to answer the overarching goal of which fuel is more efficient in a scramjet.

2. Scramjet Design and Function

2.1 Scramjet Historical Overview

As briefly mentioned before, the prospect of achieving hypersonic flight was something many engineers and scientists strived for in the late 1950s and early 1960s. Despite having the ability to use rockets to travel beyond the atmosphere and achieve high speeds, it was concluded that air breathing engines would be needed to reach hypersonic speeds with efficiency [24]. Antonio Ferri, a prominent scientist in the supersonic and hypersonic field, focused his efforts in furthering the understanding of fuel and air mixing, as well as diffusive combustion processes [12]. He also had declared four distinct differences between rocket engines and air breathing engines [24]:

1. To reiterate, the specific impulse is higher for an air breathing engine compared to a rocket engine, as shown in Fig. 1.3.
2. Considering a rocket engine and an air breathing engine with the same thrust, the latter will have higher structural weight as a result of complex intake and exhaust systems.
3. For an air breathing engine, a large thrust per frontal area occurs in a dense atmosphere as thrust is a function of the freestream Mach number and the altitude. For a rocket, a large thrust per frontal area can be obtained in a vacuum.
4. Aerodynamic lift assists an air breathing engine in maneuverability compared to a rocket engine in a vacuum, in spite of the challenges aerodynamic heating and vehicle drag bring to the structure.

Taking into account all the benefits of using an air breathing engine, specifically a scramjet, the United States decided to pursue scramjet research in the early 1960s at NASA's Langley Research Center and the Applied Physics Laboratory (APL) at John Hopkins University. There was also a notable effort of research done that the United States Air Force supported [24]. It does not imply that any studies were done previously. A study done in 1958 by Weber and McKay, which has become foundational, established that utilizing shock waves for the combustion of supersonic flow results in a decrease of pressure losses [12]. Furthermore, it was at NASA's Langley Research Center where the Hypersonic Research Engine (HRE) program was born in 1964. The objective was to provide evidence that the scramjet yielded a higher thrust than a ramjet when traveling at Mach 4-8 and develop hydrogen cooled engine structures [24]. From the program, the first iteration of the scramjet was created. Specifically, two models were designed: one using hydrogen as a coolant in an axisymmetric engine and the other was water-cooled in a pod configuration. The former was tested multiple times on the X-15A-2 and the latter was a ground-based model that resembled a gas turbine [12]. As a result of the HRE program, significant knowledge was gained regarding fuel injectors, transitioning from supersonic to subsonic combustion modes, boundary-layer transition at the inlet, and inlet-combustor and combustor-nozzle interactions [12,24]. To improve for the following iteration, it was determined that the engine should be an extension of the vehicle in order to reduce drag and achieve efficient thrust [24]. The United States was not the only country to have started scramjet research, the USSR also had its scientists and engineers focusing on issues such as, chemical conversion efficiency, heat transfer, and design operation efficiency [12].

The following iteration of the scramjet consisted of a rectangular cross-section. NASA's Langley Research Center designed a swept side-wall compression scramjet, as seen in **Figure**

2.1. It consisted of a fixed geometry that created complex inlet flow due to the sidewalls, reduced drag, and could be integrated well enough inside the bow shock of a vehicle. In addition, the swept inlet cowl granted the engine flow stability as the speed increased [12]. The aim with the swept side-wall compression scramjet was to study swept shock interactions, flow distortion at the inlet, fuel injection struts, and optimal integration with the vehicle [24].

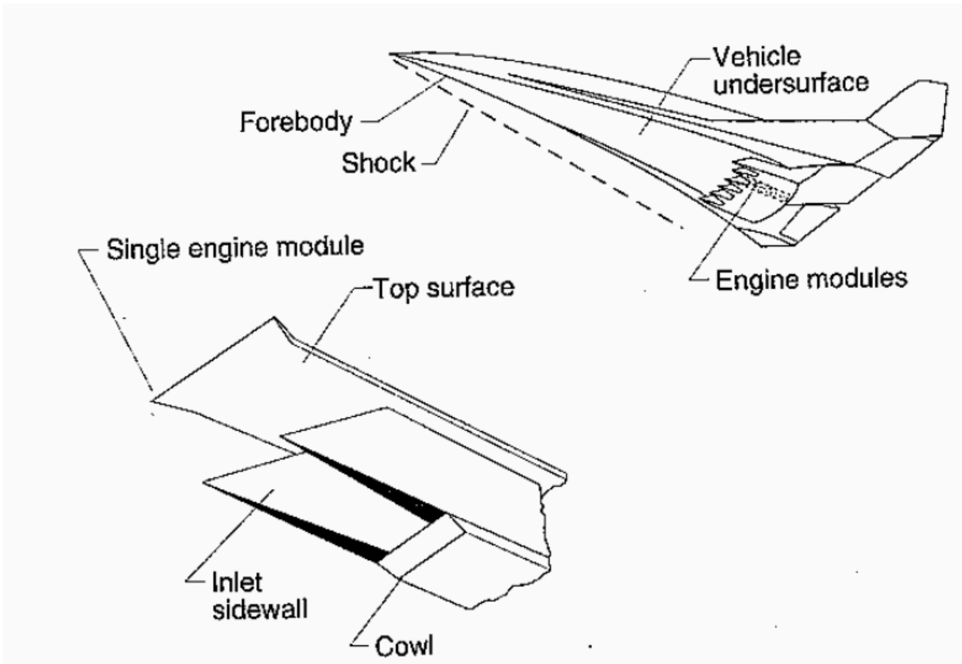

Figure 2.1 - Scramjet inlet placement [24]

As NASA's Langley Research Center focused on vehicle applications, APL directed its focus on hypersonic missile applications due to the support they received from the United States Navy. Thus, the Supersonic Combustion Ramjet Missile (SCRAM) Program was born in the early 1970s. The design consisted of a scramjet compactly placed and surrounded by the missile's components. It also included a contoured inlet to assist in starting and providing stability, as well as an isolator to prevent the inlet flow from being affected by the pressure rise due to the combustion chamber [12]. The missiles from the program were designed to travel at Mach 8 [24]. The goal of the SCRAM Program was to obtain a better understanding of the physical and chemical processes that needed for supersonic combustion, shock-train pressure rise, shock-boundary layer interactions, and serve as a database regarding inlets, fuel injectors, combusters, and nozzles [12,24].

Accumulating all the existing knowledge regarding scramjets, the National Aerospace Plane (NASP) Program emerged in 1985. The program was created with the intention of designing a single-stage-to-orbit (SSTO) vehicle that would have a horizontal launch by using a gas-turbine, use a scramjet for the transatmospheric trajectory, utilize a rocket for the low earth orbit insertion, and return with a horizontal landing [12,24]. It was the NASP Program that inspired the idea of having a reusable launch vehicle that utilized an air breathing engine, ramjet or scramjet.

During the same period, researchers in Australia were studying mixing, combustion, skin friction, shock-boundary-layer interactions, shock waves, and thrusts for scramjets in the T4 shock tunnel. They also compared the efficiency of hydrogen, hydrocarbons, and the hypergolic fuel additives [12].

Scramjets have obtained the design and efficiency they have now as a result of the dedication shown to advance and truly understand the functionality of the air breathing engine in the mid and late 1900s.

2.2 Scramjet Design

2.2.1 Inlet

For any air breathing engine, the general design guidelines that must be considered are [12]:

1. Capture exactly what is required of air for the engine.
2. Complete the required deceleration of air speed to the engine entrance while maintaining minimal pressure losses.
3. Ensure the air reaches the inlet with reasonable flow distortion while producing the least amount of drag on the system.

It is important to note that the guidelines are generalized and get more technical based on the characteristics of the air breathing engine and the overall vehicle mission objective. For instance, it is known that the effects of dynamic distortions caused by the engine entrance on the gas-turbine compressor are severe as it can reduce the stall margin. The same cannot be said regarding scramjets, as there are two possibilities for dynamic distortions: mixing could be accelerated as a result of the flow unsteadiness or there could be unfavorable effects on momentum losses. Another consideration that must be given for scramjet inlets is cooling, to handle the increase in temperature [12].

Some expected characteristics for a scramjet inlet include, but are not limited, to the following [12]:

1. Compressing working fluid using inlet geometry, which will result in a 3D shock-wave train throughout the isolator before reaching the combustion chamber.
2. Utilize variable geometry, which will allow the engine to meet flow-rate requirements as it transitions from supersonic to hypersonic speeds.
3. Be compatible with pressure rises in the combustion chamber.
4. Optimal integration with the fuselage due to the long compression ramps.
5. Composed of a single segment or multiple segments, where the exact amount is dependent on the dimensions of the vehicle and frontal area of the propulsion system.

Referring to the first characteristic to consider, the largest driving factor in scramjet inlet design is the type of compression desired. This is to ensure that there is minimal pressure loss up until the combustor. The three inlet design categories are external compression, mixed compression, as seen in **Figure 2.2**.

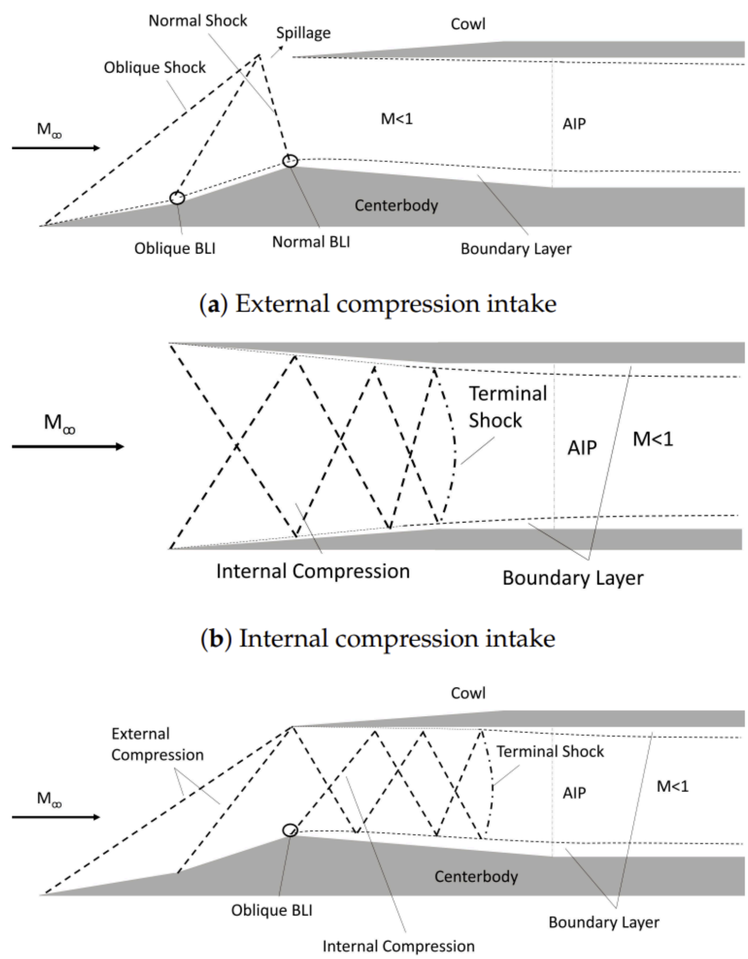

(**a**) External compression intake

(**b**) Internal compression intake

(**c**) Mixed compression intake

Figure 2.2 - Different inlet compressions [25]

As the name entails, the difference is ultimately where the compression occurs in regards to the geometry of the vehicle and the scramjet inlet. For external compression, the scramjet is self-starting, meaning that it will spill flow until it reaches the design Mach number. For mixed compression, shocks occur externally and internally. External drag can be minimized by ensuring that the external cowl angle corresponding to the freestream is extremely small. The scramjet is also self-starting, however what also makes it differ from external compression, is that it is longer in length. In addition, variable geometry may be needed, and the specifics can be determined by the amount of internal compression. Internal compression inlets are relatively shorter than mixed compression inlets. A downside of utilizing such inlets is the difficulty in integrating it with the vehicle. Internal compression inlets capture all the incoming flow, compared to the flow spillage of external and mixed compression inlets. Whereas mixed compression inlets may require variable geometry to start, internal compression inlets will always require variable geometry to start [4]. As depicted in **Figure 2.2**, all compression categories include a variation of oblique shock waves and normal shock waves.

The efficiency of the combustion chamber is dependent on the properties of the incoming air, i.e. the flight conditions. Considering that the scramjet requires, at minimum, supersonic speeds to function in its entirety, great consideration must be given to the design of the inlet to ensure said function. Research in optimizing the scramjet inlet is plenty. To ensure minimal pressure loss, Siddiqui and Ahmed [26] offer three ways to compress the free stream air flow to achieve such a goal, external, mixed, and internal compression as mentioned above. Most analysis done for designing the inlet considers 1-dimensional flow, therefore considering a mixture of compression waves between the forebody and the inlet is an easier way to start. This results in designing a cowl, which is the bottom exterior of the engine, to be parallel to the freestream flow and produce minimal entropy increase [26]. Siddiqui and Ahmed [26] begin their process by calculating the ratio between the area a certain axial distance from the forebody to the beginning of the inlet. Once that area ratio is calculated, and knowing the height of the inlet from the design of the combustor, they are able to calculate the height of the corresponding axial distance considered before. The height is needed as it will determine how far apart each oblique shockwave needs to be to produce the desired static pressure and static temperature ratios [26]. The findings of [26] regarding the axial distances of four oblique shockwaves resulted in a total length of 3.19 meters for a freestream Mach of 4, which can be seen in detail in **Figure 2.3**.

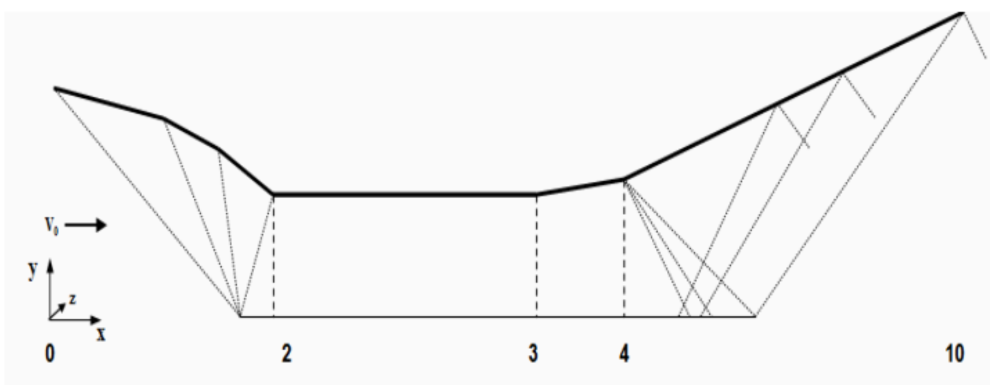

Figure 2.3 - Inlet design for scramjet [26]

Alhassani et al. [27] use of ANSYS software for computational fluid dynamics (CFD) simulations to analyze the conceptual scramjet intake designs. The study varies two parameters: the inlet diameter and the angle of the fins. The simulations aim to minimize pressure losses and improve efficiency [27]. Refer to the results section of [27] for the CFD results for different intake configurations. The study observes the development of oblique shock waves and their interactions with the boundary layer. The findings suggest that increasing the channel width enhances oblique wave generation, while decreasing the fin inclination angle also improves oblique wave interactions. The optimal combination is identified as a diameter of 1.75 m and an inclination angle of 15 degrees at the leading edge of the forebody. The study highlights the importance of inlet design in achieving effective combustion and reducing pressure losses. The findings provide valuable insights for future experimental validations and further optimizations of scramjet propulsion systems [27].

A different approach is considered in Anderson [28]. Instead of considering multiple oblique shockwaves either before or within the inlet, it focuses on one isentropic compression wave formed at the leading edge of the forebody. The difference is that the compression wave follows a similar process of a Prandtl-Meyer expansion wave, since it is the opposite of the expansion wave. Through Example 9.10, it is found that an isentropic compression wave is more efficient in pressure loss compared to an oblique shockwave. The pressure after a compression wave was 18.02 atm, whereas the pressure after an oblique shockwave was 13.32 atm. A 5 atm pressure difference is all enough to affect the speed of the overall scramjet. It is an interesting observation that all the sources mentioned before consider oblique shockwaves, implying sharp corners. To have an isentropic compression wave, the corner must be smoothed out.

All the sources above mention that it is important to minimize the pressure loss at the end of the inlet design, which then applies to the entrance of the combustion chamber. Araújo et al. [29] explains in further detail how this pressure loss should be optimized considering the SCRAMjet inlet design. Plenty optimization methods were mentioned, from Heiser and Pratt, Anderson, and Oswatitsch to name a few. What all have in common is that the temperature, pressure, and Mach number from the freestream flow plays a crucial role in the resulting temperature, Mach number, and pressure leaving the inlet. The methodology given in [29] gives equations that are a function of the number of oblique shockwaves. In addition, most of the optimization methods consider a mixed compression system where there are oblique shockwaves between the entrance of the forebody and the inside of the inlet. Two parameters, or criteria, that previous sources did not include were the Korkegi limit and shock on-lip and shock on-corner conditions. The Korkegi limit describes the critical pressure ratio where flow separation will begin to occur as a function of the freestream mach number. Part of the inlet design is to ensure that the pressure ratio does not exceed the Koregi limit. The shock on-lip and shock on-corner describe the distance external shockwaves, from forebody to inlet, and internal shockwaves, inlet entrance to exit, must have in order to maximize mass airflow. Considering all these specifications, Araújo et al. [29] found that the oblique shock waves should occur at angle of 6.008◦, 7.077◦, and 8.387◦, resulting in three inlet ramps and not sharp corners as seen in **Figure 2.4**.

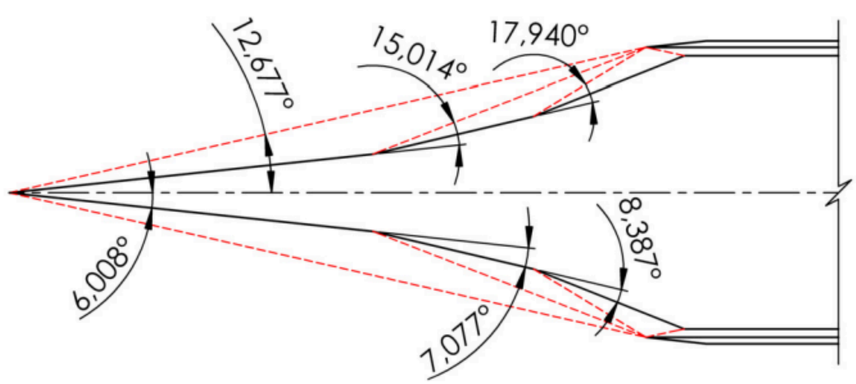

Figure 2.4 - Inlet ramp configuration [29]

The angles will optimize pressure loss, resulting in the combustion chamber producing the larger pressure and temperature difference. Araújo et al. [29] provides excellent information to consider if the goal is to study the optimization of solely the scramjet inlet, which is not the center of this thesis.

While all the sources focus on the type of waves needed, the boundary layer, increased temperatures, and energy of the airflow need serious consideration as well. To ensure that the scramjet will be operable throughout the flight regime and have a high performance, the boundary layer formed will need to be controlled [12]. **Figure 2.2** depicts the boundary layers formed as a result of shock waves, further demonstrating that complex analysis required. In addition to the cooling methods mentioned above, the material at the inlet should also be given serious thought as it will also determine how much heat it can withstand based on the compression done. Ultimately, the unification of the inlet and the thermodynamic cycle chosen for the scramjet becomes of import for hypersonic speeds [12]. As the airflow is entering the inlet, the energy present can be beneficial, yet also disadvantageous. If a combined thermodynamic cycle is considered, then cryogenic fuels can assist by storing a portion of the incoming airflow. Yet, the exact amount of the supplementary energy that the fuel can afford to give is limited by the large air energy content. If magnetic fields were considered to decelerate the flow, a magnetohydrodynamic process could bypass a certain amount of said energy throughout the scramjet. However, additional components would be required, and the weight added would have to be determined worthy or not. Furthermore, magnetohydrodynamic processes also deposit energy in the inlet and are contemplated as they assist in controlling shock-wave structure, as well as mass-flow capture [12].

2.2.2 Isolator

Regardless of the type of compression the scramjet inlet utilizes, the result is the same: shock waves will decelerate the flow and increase the pressure and temperature as it prepares to enter the combustion chamber [30]. As the fuel is mixed with the incoming air and combusts, there will be a large local pressure rise, and the boundary layer on the surfaces will begin to separate. It is the latter that will begin to cause difficulties as the boundary layer separation can feed upstream and generate a shock-train, which in turn will result in the flow being further compressed. Thus, enters the isolator, as it is located between the inlet and the combustion chamber. Its location prevents the negative effects that comes with boundary layer separation and allows the incoming flow from the inlet to continue as was. That does not imply that the isolator does not contain any boundary layer. The incoming air flow creates a boundary layer due to the supersonic speed it is entering at and the geometry of the inlet and isolator. The boundary layer produces either normal or oblique shock waves that span over the length of a majority of the isolator, which is where the shock train originates from. The shock train is what allows the pressure to further increase without introducing negative effects Furthermore, there is also a mixing region that forms between the incoming flow and the separated flow. The mixing region balances the pressure rise in the incoming flow in opposition to the shear stress of the boundary layer. Eventually, the incoming flow will reattach to the surfaces of the isolator, matching the expected conditions entering the combustion chamber. Ultimately, determining the length of the flow structure in the isolator is an important design characteristic as it reveals where unfavorable behaviors begin to develop and where to stop [30].

There are different types of physical behavior that can occur in the isolator as a function of Mach number, depicted in **Figure 2.5**.

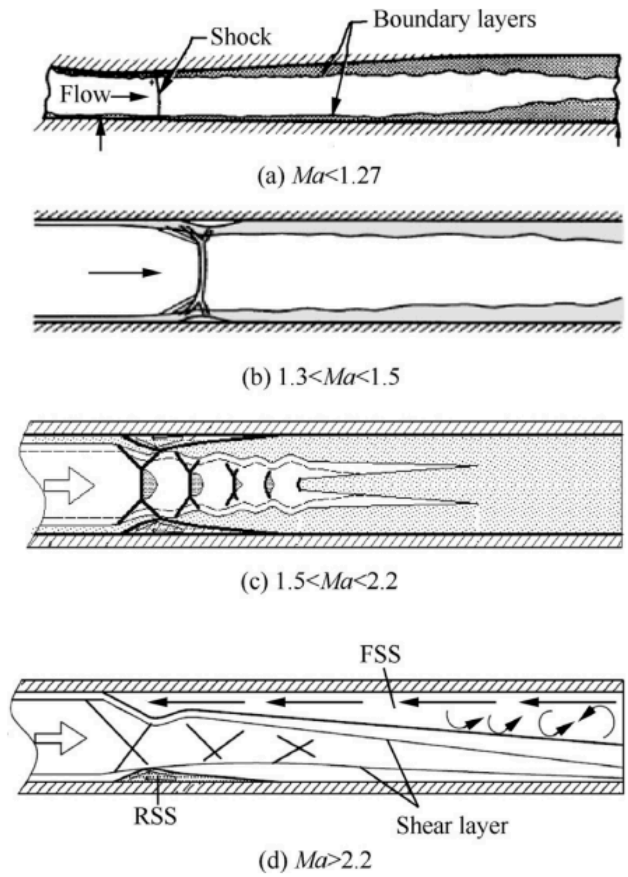

Figure 2.5 - Shock and shock trains as a function mach number [31]

Since the center of discussion are scramjets, only **Figure 2.5(c)** and **Figure 2.5(d)** are relevant for discussion. **Figure 2.5(c)** displays a normal shock wave train, which occurs in the low Mach regime that scramjets can operate in. **Figure 2.5(d)** displays an oblique shock wave train, which is more common to expect and analyze as scramjets tend to travel at freestream Mach numbers higher than 2.2 [31].

2.2.3 Combustion Chamber

The combustion chamber, or the combustor, is the segment that proceeds the isolator and the heart of the scramjet. In a general sense, the combustion chamber follows an exothermic chemical process where fuel is injected, mixes with the incoming air, and then combusts due to a combination of the high static temperature and pressure of the incoming air and some kind of igniting device. It is important to note the incoming air has to be supersonic as it makes its way to the combustion chamber as having anything faster increases the chances of dissociation of the air, which results in unacceptable thermal loads. Also, the time allocated, also known as the residence time, for the combustion process to complete is very small due to the speed at which the incoming air is traveling. For instance, if a 0.5 meter combustion chamber is considered and flow is traveling at 2165 meters per second, the residence time is 0.23 milliseconds. Thus, there is a small margin for error and design needs to be as efficient as possible [32].

Musielak [32] mentions some properties to consider when designing a combustion chamber:

1. Ideal combustion efficiency (η_b) of 100%, indicating complete combustion.
2. Ideal combustor total pressure ratio (π_b) of 1.0, indicating a low total pressure loss
3. Ensuring combustion stability by limiting perturbations from growing to the extent features of the incoming flow will be altered.
4. Ensuring a slight change in temperature as the flow enters the exhaust nozzle.
5. Including a small cross-section and short length to lessen any internal drag and decrease the overall weight of the engine.
6. Ensuring a form of re-ignition in case there is a flameout.
7. Ensuring the engine can operate in various flight conditions that lead to different mass flow rates, pressures, and temperatures.

Concerning parameter four, the combustion stability, the scramjet is susceptible to two types of combustion processes, mixing controlled and kinetically controlled. The former is when the combustion rate is a function of the rate at which the fuel and the incoming flow mix. The latter is when the combustion rate is a function of the rate of chemical reaction occurring between the fuel and the incoming flow. Ideally, mixing control should be maintained throughout the combustion chamber. Realistically, the flow upstream is kinetically controlled and is more prominent for high Mach numbers. It implies that the ignition delay times have the same magnitude as the fluid scale [9]. As a general rule, considering the mixing and combustion timescales is a necessity in order to define the flow processes and optimize the design. Musielak [32] also includes processes that are important in scramjet design: fuel injection, fuel and air mixing, ignition, flameholding, propagation, and stabilization, transition from subsonic to supersonic flow combustion, thermal choking, and interactions, such as inlet pressures, spillage, unstarting, within the engine inlet and the exhaust nozzle.

To examine the combustion chamber entrance conditions, there are two important variables to consider:

Combustion Chamber Entrance Pressure: As the incoming air is decelerated at the inlet by compression, and then further decelerated within the inlet, the pressure at the entrance of the combustion chamber is expected to be extremely high. It is crucial that it maintains a large magnitude as it will ensure that the air and fuel will mix completely within the given combustion chamber span, affecting the combustion efficiency. Said chamber has high heat and structural loads and therefore, the length should be very small. In the case that the pressure at the entrance is very low, the combustion chamber entrance will have to increase in length in order Musielak [32].

Combustion Chamber Entrance Temperature: It has been mentioned plenty that the temperature at the entrance of the combustion chamber should be high. There is a limit to the magnitude of that temperature. To determine the exact maximum value, complex analysis is required, including parameters such as flight altitude, flight Mach number, inlet losses, type of fuel, fuel-to-air ratio, combustor, and nozzle geometry [32]. Fortunately, Musielak [32] provides an estimate for a scramjet. The minimum temperature required to ensure hydrogen, if chosen as a fuel, ignites is approximately 845 K. Yet, the temperature cannot reach a value that is extremely high, resulting in air dissociation. It will reduce the thermodynamic cycle efficiency. Another parameter that is considered. Assuming that the inlet is effectively compressing the incoming air with weak shock waves, a reduced static temperature rise will be provided. The temperature for disassociation for molecular oxygen is known to be around 2000 K. Taking into account all the assumptions and known values, the estimated maximum combustion entrance temperature is between 1440 K and 1670 K. The range can change as this is, to reiterate, dependent on the flight condition and the rest of the scramjet design [32].

While there are many variables to consider when analyzing the flow field of the combustion chamber, one that is rather simple to control and zoom into are the fuel injectors. The overall goal for an efficient fuel injection is to disperse the fuel evenly, while making certain that the mixing is occurring at a fast rate within the span of the combustion chamber. There should also be a section within the combustion chamber for flameholding while maintaining a minimum total pressure loss and internal drag. Flameholding is the process required to ensure that the combustion process continues as the flow is mixing. Regarding the type of fuel injectors to use, there are a variety of structures to choose from. Orifices or slots on the combustion chamber walls, ramps, strut injectors, to name a few [9,12]. Which to use is dependent on the flight conditions and the desired efficiency. For example, flight Mach numbers up to 10 allow the fuel to be injected with a normal component. For flight Mach numbers exceeding 10, it is ideal to have most of the fuel injected axially as it will carry momentum responsible for a majority of the thrust [12]. The most straightforward method for fuel injection is transverse fuel injection from orifices on the combustion chamber wall. Utilizing such a method allows for rapid mixing with the nearby field and adequate fuel penetration. Moreover, mixing can also be improved by introducing the aerodynamic phenomenon, vorticity, via wall injectors with geometrical designs or wedge shaped devices placed on the combustion chamber walls. Scramjets often opt to use fuel injection ramps or in-stream struts. Ramps have the fuel injected streamwise from the base and introduce streamwise vorticity in the flow. Yet between the two configurations of ramps, unswept and swept, the latter is favored as a result of generating better axial vorticity and mixing [12]. In-stream struts, which inject fuel in a transverse direction, are more efficient when streamwise injection is also considered. More recent injector designs include pulsed injectors and fuel injection integrated with cavities. Pulse injectors can use mechanical devices, oscillation techniques, or shuttering techniques. Having fuel injection integrated with a cavity also supplies flame stabilization, flameholding, and better mixing if designed correctly [12].

Despite the scramjet combustion chamber geometry being simple, the turbulent combustion flow field that evolves is intricate. This is a consequence of simultaneous fuel injection, having air and fuel mixing occurring over thick boundary layers, interconnected shocks, the ignition that depends on the chemical kinetics of the species in the mixture, and aerothermodynamic processes. Hence, to accurately describe the flow field, fuel injection, fuel jet penetration, fuel and air mixing, ignition and chemical reaction, turbulent burning, flame structure, flameholding, and thermal choking need to be examined [32].

The combustion chamber has only been briefly described, yet displays its multifaceted, complex nature. Studies concerning the combustion chamber are still on-going as there is only so much analysis that can be done with today's technology in attempts to optimize its performance. The results of the study conducted by Stalker et al. [33] have served as a basis to translate similar designs to a scramjet. The goal was to examine the effect hydrogen combustion has on the boundary layer in order to understand surface friction reduction and heat transfer using the configuration in **Figure 2.6**. The hydrogen was injected by a slot that spanned the entirety of the width of the duct. They assumed the air composition to be 76.6% N_2 and 23.4% O_2 for one of their cases. The experiment variables were fuel input and four different injection conditions. The results demonstrated that there are reductions in the shear friction as a result of the hydrogen combustion in the boundary layer.

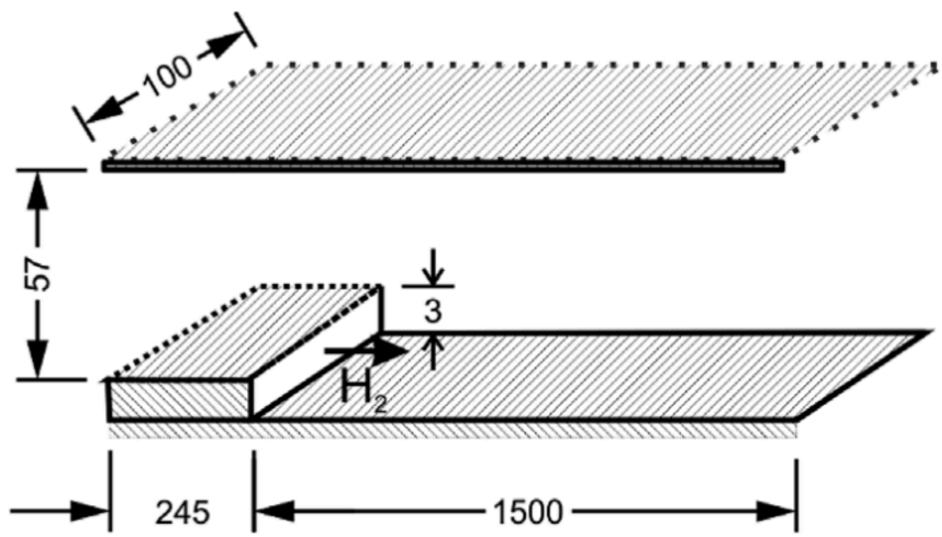

Figure 2.6 - Back step fuel injection for scramjet [33]

Another study was done by Waidmann et al. [33] utilizing the configuration in **Figure 2.7**. Hydrogen was injected parallel to the incoming flow at a sonic speed via a strut. By the nature of the strut, extra shock waves were formed at the leading edge of the strut and near wake region. These shock waves improved the fuel-to-air mixing in the vicinity of the edge of the strut. Despite the increase in combustion being a product of shock-boundary layer interactions, it was found that the interaction between the viscous and inviscid parts of the flow resulted in total pressure loss. Regardless of the results, the study has still proven helpful to the community as it serves for verification for the physics of similar designs.

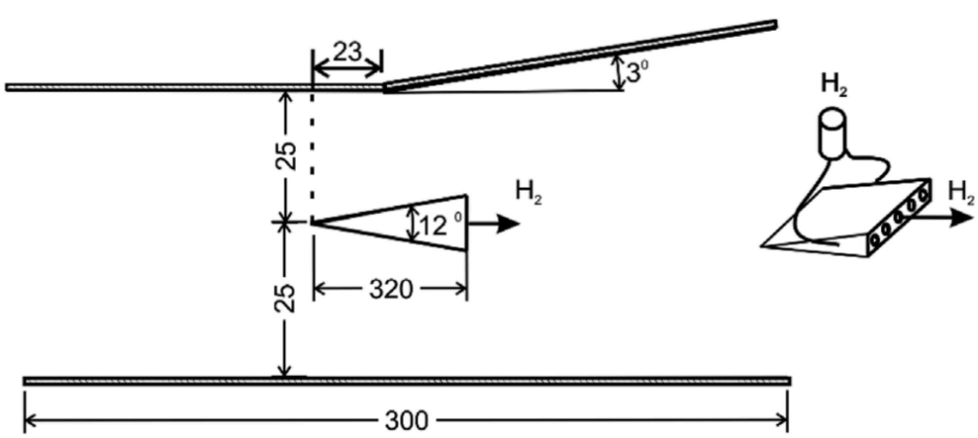

Figure 2.7 - Strut fuel injection for scramjet [33]

2.2.4 Exhaust Nozzle

The exhaust nozzle is the fourth and final part of the scramjet engine. The overall goal of the nozzle is to use the difference in pressure from the flow exiting the combustion chamber to the atmospheric pressure as a means to provide thrust for the vehicle. As per the other parts of the scramjet, it is ideal that there be minimum losses and the nozzle has been optimized for maximum thrust. Since a large nozzle pressure ratio is required in order for a hypersonic vehicle to propel forward, there needs to be a long nozzle. To prevent adding weight to the scramjet engine itself, the aftbody of the vehicle serves as part of the nozzle, known as a Single Expansion Ramp Nozzle (SERN). For instance, NASA's X-43 displayed a similar design to **Figure 2.8**. This means that for a scramjet with no combined cycles, the thermodynamic cycle can be considered open. When designing the scramjet engine and the vehicle that it will be integrated with, maximum stability and having a low trim drag is desired as the aftbody of the vehicle can be responsible for large forces and moments [12,32].

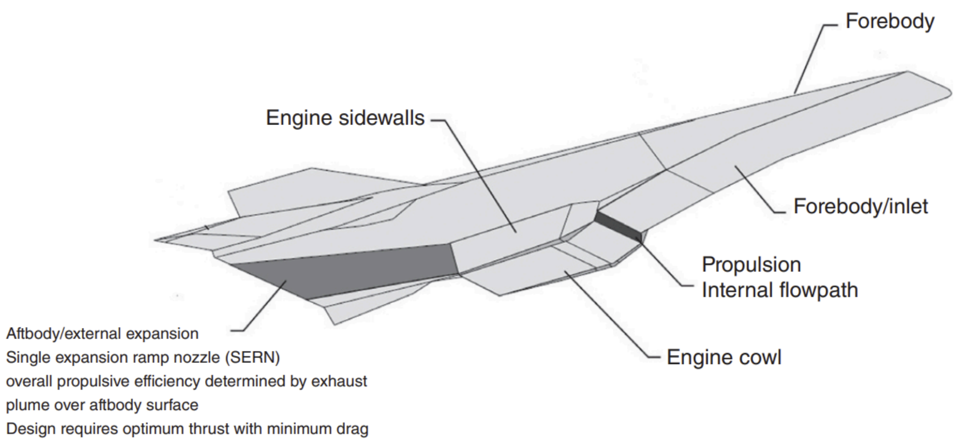

Figure 2.8 - Exhaust nozzle location [32]

When analyzing the expansion process, it should be noted that the flow field is not entirely supersonic when traveling at supersonic or hypersonic speeds since there are thin boundary layers near the nozzle surfaces. The high temperature gas within the nozzle and the surrounding air combine with one another by means of shear layers in the exhaust flow, which can be considered the plane of symmetry for a symmetric 2-D nozzle. The symmetric 2-D nozzle can become a 3-D nozzle when the large pressure gradient between the cowl and shear layer causes the latter to bend either inward or outward [32].

When the nozzle begins to deviate from its intended design, there are two outcomes: overexpanded or underexpanded flow. Overexpanded flow occurs when the static pressure leaving the nozzle is less than the atmospheric pressure, leading to the formation of a shock at the edge of the nozzle cowl. To handle the large atmospheric pressure, the exhaust stream handles the large atmospheric pressure via a shock diamond wave structure. The stability and trim are put at risk due to the unfortunate change in flow conditions. Underexpanded flow occurs when the static pressure leaving the nozzle continues to increase and is higher than the atmospheric pressure. When a jet expands and interacts with an external flow, a lip shock forms at the jet's edge, and a contact discontinuity separates the jet from the surrounding air [32].

The exact design of the SERN can be seen in **Figure 2.9**. There are four major components: the internal upstream, contour, an expansion ramp, two sidewalls, and a cowl. There is a choice to have the expansion ramp curved or straight, which would determine the values of β and θ. As for the portion of the cowl past the throat of the converging-diverging nozzle, it can be short, long, straight, or turned upward. The nozzle internal expansion ratio and the nozzle performance are a function of the design of the four sections. While using the SERN reduces the weight of the scramjet and the skin friction drag, it underperforms when the vehicle is traveling at transonic and hypersonic speeds. The flow is overexpanded since the nozzle is not producing a high enough pressure, resulting in the exhaust mass flow insufficiently filling the large area ratio [32].

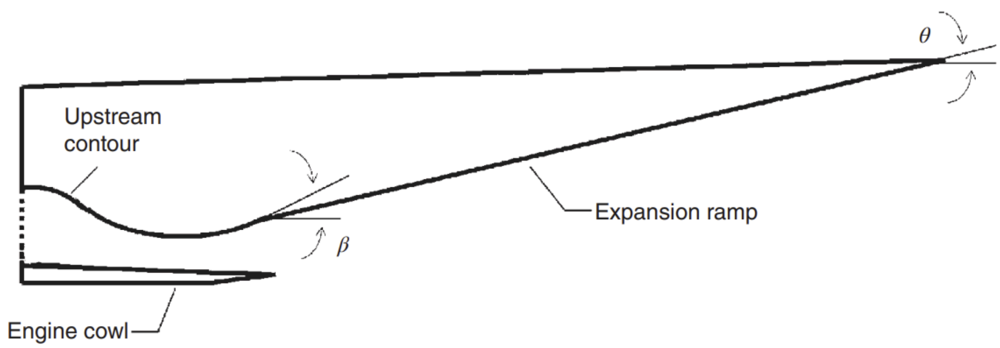

Figure 2.9 - Simple expansion ramp nozzle design [32]

The efficiency of the nozzle is affected by two major parameters: the design of the nozzle itself and the flow characteristics at the end of the combustion chamber. A leading source of loss is wall friction in the nozzle, which can lose up to 2% of ideal thrust. If there is too much divergence, the flow can stray from its ideal axial orientation resulting in further losses. The flow non uniformities, adding to the thrust losses, at the nozzle entrance are a function of the inlet efficiency and any flow distortions after the incoming flow was compressed, fuel injection, mixing and combustion efficiency, development of boundary-layers, and shock-boundary layers. Lastly, the concern of dissociation from the combustion chamber carries over to the nozzle. The sudden expansion can cause the flow to freeze, and result in energy loss as the chance for recombination is diminished [12,32].

2.3 Scramjet Geometry

2.3.1 CIAM/NASA Scramjet Configuration

The purpose of this project is to study the effect different reaction mechanisms have on the performance of a scramjet, and not the configuration of the scramjet itself. For that purpose, the design of the Central Institute of Aviation Motors (CIAM) scramjet is utilized. CIAM designed an axisymmetric scramjet that was integrated with a SA-5 surface-to-air missile, achieving a Mach range of 3.5 to 6.4. Making adjustments to the original model, CIAM conducted more tests. The first test reached a Mach number of approximately 5.5. The second and third test, coordinated with the French government and French businesses, achieved a Mach number of 5.35 and 5.8, respectively. It was in 1994, and after the three tests took place, that NASA made a contract with the Russian CIAM, allowing another modified axisymmetric, dual-mode scramjet to be used for ground and flight tests at Mach 6.5. The aim of the contract was to have experimental supersonic combustion flight data and provide flight-to-ground data to be utilized for design verification [34].

The geometry was taken from McClinton et al. [34]. **Figure 2.10** represents the inlet ramp and the isolator. **Figure 2.10** represents the combustion chamber and the beginning of the nozzle. There is not much information regarding the nature of the nozzle. From **Figure 2.10**, the angle at which the cowl's trailing edge tips down is assumed to be 30 degrees. Additionally, **Figure 2.11** includes the pylons utilized for the scramjet as well as the fuel injector locations. These parts were neglected as they do not significantly affect the reaction mechanisms. The main focus is only the overall space in which the reaction mechanisms will be contained to. It is important to note that Voland et al. [35] and Roudakov et al. [36] also include the design of the CIAM/NASA scramjet, and can be used as a reference. However, McClinton et al. [34] includes the most dimensions on the scramjet and is easier to follow in replicating the scramjet.

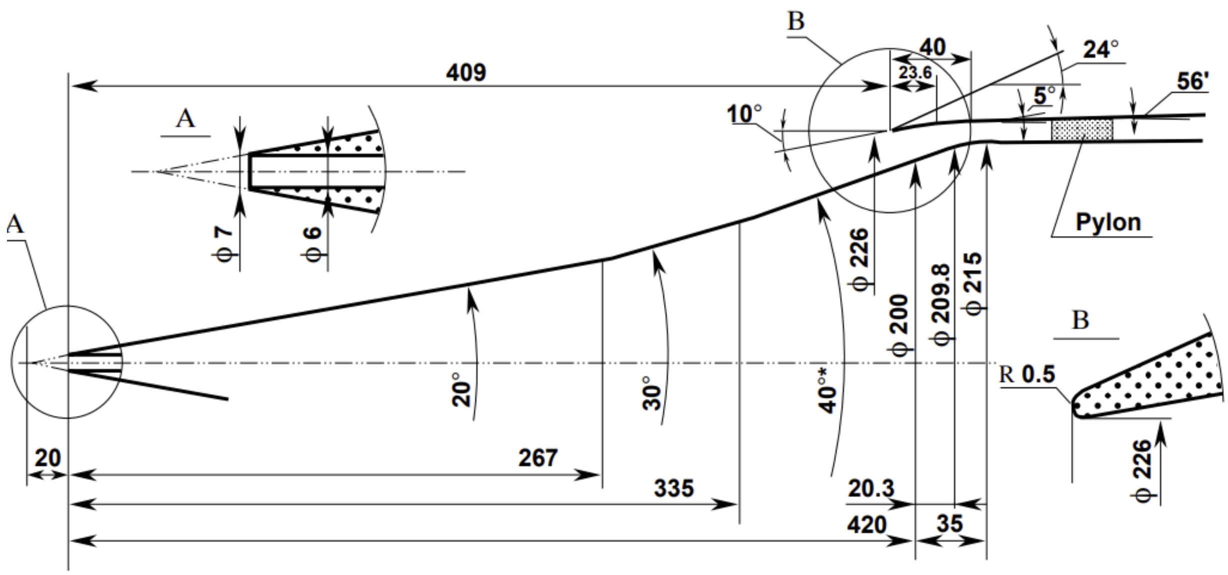

Figure 2.10 - CIAM/NASA scramjet inlet geometry [35]

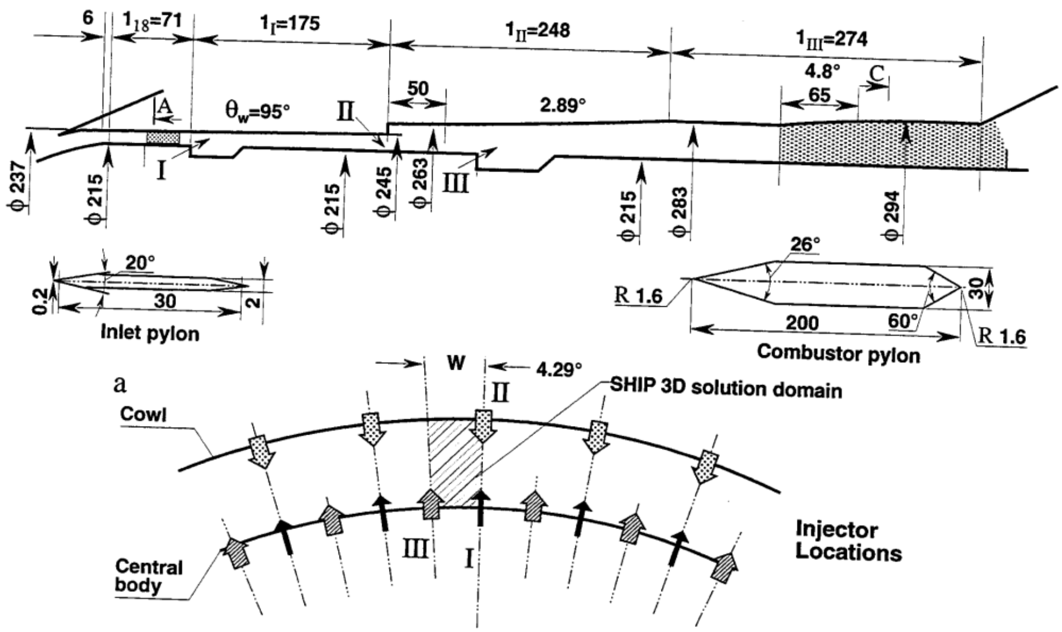

Figure 2.11 - CIAM/NASA scramjet isolator and combustion chamber design [34]

2.3.2 CIAM/NASA Scramjet CAD

The software utilized for the computer aided design (CAD) of the CIAM/NASA was SOLIDWORKS Student Edition 2025, yet any version available is fine. Any other CAD software is welcomed, whichever is easier to access and maneuver. Roudakiv et al. [36] do include the width dimensions for the scramjet, thus allowing for a 3-D design. This project focuses mainly on a 2-D design as multiple reaction mechanisms will be analyzed and allow for a more reasonable timeframe to achieve the goal. In **Figure 2.12**, A represents the inlet, B represents the isolator, C represents the combustion chamber, and D represents the start of the nozzle. All dimensions are in millimeters. While most of the dimensions are given in [34-36], there are some intricate details that are not described and therefore algebraic and trigonometric methods were used to make estimations based on existing values.

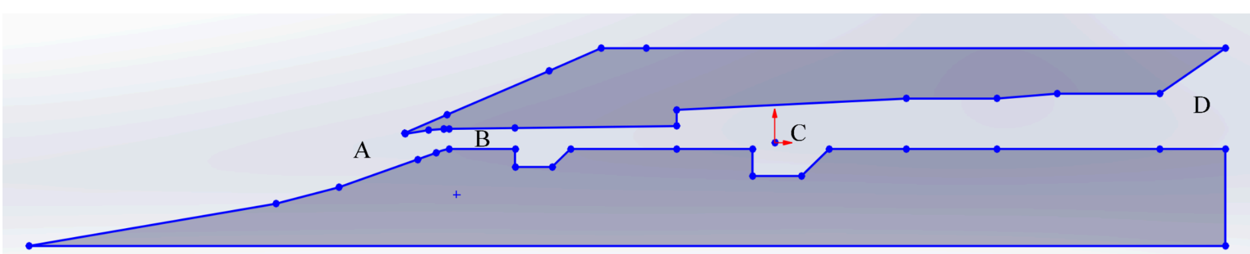

Figure 2.12 - CIAM/NASA axisymmetric dual-mode scramjet CAD

3. Scramjet CFD Verification

The overall goal of this section is to utilize the CAD of the CIAM/NASA scramjet, perform CFD in ANSYS Fluent to simulate the flow path traveling through the scramjet, and validate the results obtained against published inlet data from McClinton et. al[34].

For simplicity, ANSYS Fluent and ANSYS Mechanical will be referred to as Fluent and Mechanical, respectively, moving forward.

3.1 Preprocessing and Mesh Generation

3.1.1 Geometry Preparation and Import

In order to accomplish the goal of this section, the CAD model discussed in Section 2.3 was adjusted. If the model displayed in **Figure 2.12** were to be imported into Fluent, the solid components such as the cowl and lower half of the aircraft would be analyzed, which is the opposite of the proposed objective. The canal between the cowl and the part of the engine that is attached to the body needs to be solid in order to be imported into Fluent, as displayed in **Figure 3.1**.

Figure 3.1 - Adjusted CIAM/NASA scramjet CAD

The rectangular domain, depicted by the solid grey area, is necessary as it reflects the open space of the flow. To ensure that Fluent would be able to run an axisymmetric simulation, the bottom and vertical edge of the engine was neglected.

The next step is to export the CAD model as a .STEP file. This allows for easy uploading to Fluent and prevents any errors in the geometry as it is transferred.

Simplifications to the geometry could be made, such as removing any small features or ensuring symmetry. This would allow for mesh creation with minimal error and have the mesh be uniform across the domain. However, the CAD model was kept as close to the original design by CIAM/NASA in order to get results as accurate as possible.

3.1.2 Meshing

Mechanical considers the 2D CAD of the scramjet as a sheet body. As a result, it automatically chooses a quad dominant sheet body method, where it uses quadrilateral elements to create the mesh. Most of the elements are squares due to the element size chosen. However, in certain areas, the quadrilaterals can be seen in **Figure 3.2**. This is particularly beneficial as it will capture the physics at the cowl tip and the overall canal of the scramjet since the former is curved and the latter is relatively thin.

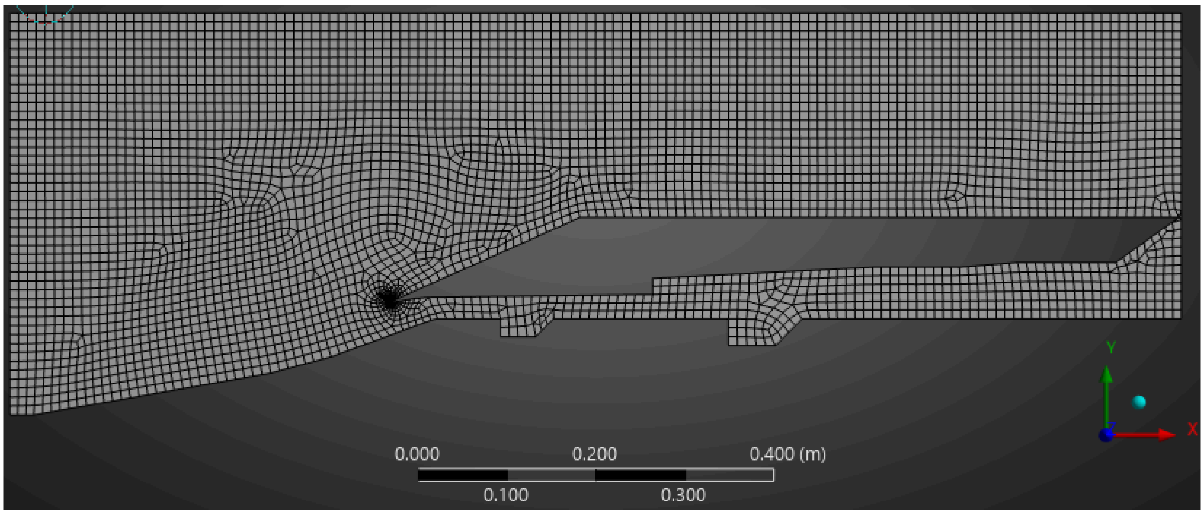

Figure 3.2 - CIAM/NASA scramjet mesh

Typically, to obtain accurate results a fine mesh is considered. Yet, the computing time is significantly increased when attempting to do so. Since we are considering hypersonic speed, which includes turbulent flow, it is beneficial to have fine mesh at the boundary layers to capture all the physics that is occurring, as is demonstrated by the darker regions in the canal in **Figure 3.2**. Choosing to only have a fine mesh at the boundary of the scramjet reduces the computational time than if doing the overall domain, while capturing the boundary layer behavior. In Mechanical, you can choose which parts of the geometry to focus the mesh on. All internal edges, such as the inlet ramp, the cowl tip, the isolator, the combustion chamber, and the nozzle, were selected. This edge sizing, as Mechanical calls it, results in **Figure 3.3**, where along the boundary layers, the mesh appears more concentrated than the surrounding area. Another concentrated area is the cowl tip, which is to be expected as it is the only part in the scramjet that is curved, and thus requires more elements.

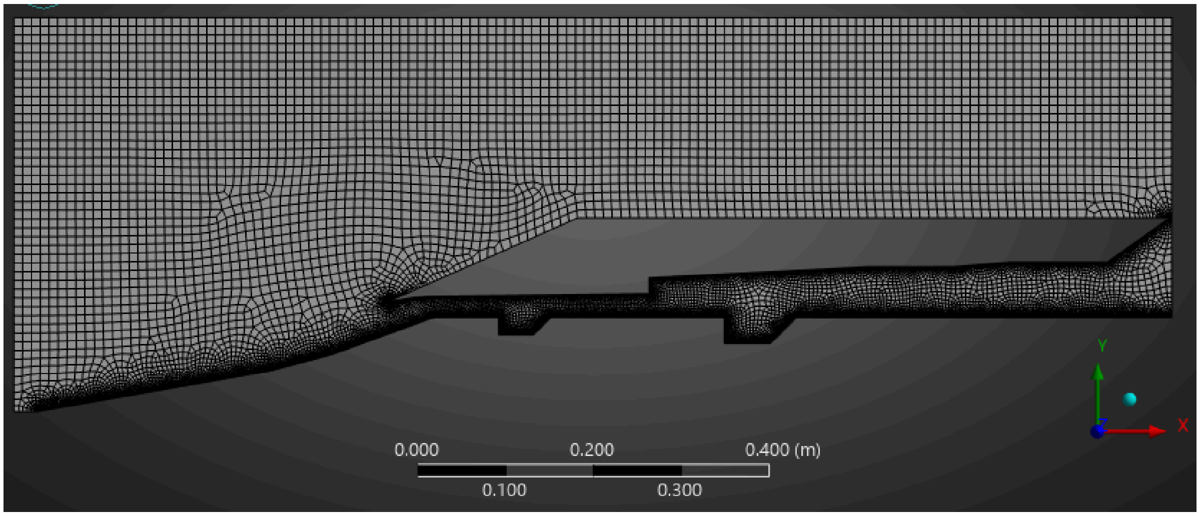

Figure 3.3 - Face and edge sizing mesh

Detailed information regarding overall mesh information can be found in Table 3.1.

Table 3.1 - General mesh information

Parameter	Value
Growth Rate	1.2
Transition Ratio	0.272
Target Skewness	0.9
Orthogonal Quality	> 0.36744
Max Aspect Ratio	5.247
Nodes	22,072
Elements	20,669

The number of elements and the element size considered for the verification is relatively low due to available computing power. This will be modified when analyzing the reaction mechanisms.

Another key step when meshing is to create labels for the geometry. As this project considers a 2D scramjet, the edges of the entire CAD were labeled. For instance, the inlet, i.e. where the incoming flow is entering, was selected as the left and upper edges of the rectangular domain. The outlet was selected as the right edge of the rectangular domain. The internal edges, i.e. where the canal is located, were named as their corresponding parts. The outer walls of the scramjet were named as outer walls. As an axisymmetrical plane will be considered, an axis needs to be defined in order for Fluent to know about which axis to revolve about. There is a small segment right before the inlet ramp, and it was labeled axis. Creating names for the geometry allows Fluent to automatically recognize it as boundaries and set up the corresponding boundary conditions for the different geometry parts.

3.2 Boundary Conditions and Simulation Set Up

This subsection will follow the order of the menu in Fluent for efficient followthrough.

3.2.1 General Task Page

The general page is where the user sets up the solver settings. Under the type, a density-based solver is chosen as the fluid flow considered for this project is high-speed and compressible. This allows Fluent to solve the mass, momentum, and energy conservation equations as a coupled set. The velocity formulation can stay as default. The time can be left as steady as this is only a verification run. The 2D space can be set to be axisymmetric. Axisymmetric is considered as the realistic geometry of the CIAM/NASA Scramjet is conical. Attempting to proceed with 3D CFD would require a high power computer that will be able to tolerate the computational intensity, a large storage to save the large datasets, and allocating enough time to run lengthy simulations. Thus, the side profile is considered and then split in half horizontally to avoid the complications that come with 3D geometry.

3.2.2 Model Selection

In order to obtain accurate pressure, temperature, and Mach number results for a hypersonic flow, turbulence must be considered. The turbulence model used in Fluent is the Shear-Stress Transport (SST) k-ω viscous model with the production limiter. The default values provided by Fluent remained unchanged. The energy equation is also selected. A more detailed description of the turbulence model and energy equation can be found in Section 3.3.

3.2.3 Material Selection

Air is the working fluid whenever analyzing a scramjet. By default, Fluent considers the density to be constant. In order to replicate the real-life conditions of a scramjet, density is changed to an ideal gas, which Fluent considers to be real and compressible. As a result, Fluent will then provide options for specific heat at constant pressure, thermal conductivity, viscosity, and molecular weight. The default values Fluent has can be modified to piece-wise polynomial, constant, Sutherland's, and constant, respectively. Thermal conductivity is kept constant as this project does not focus on the thermal analysis of the material of the scramjet and the effects it may have on the walls.

3.2.4 Boundary Conditions

McClinton et al. [34] provide the free stream Mach number and the altitude at which the scramjet is tested to be 6.5 and 26 km, respectively. Given the altitude, [37] is used with linear interpolation to calculate the temperature and pressure, which was found to be 222.54 K and 2163.2 Pa, respectively. With the free stream conditions determined, the type in Fluent for the inlet to be pressure far-field since the conditions away from the inlet are known. It is significant to observe that since the scramjet is traveling at a Mach number much greater than 0.1, the gauge pressure can be considered the same as the free stream, or static, pressure.

In Fluent, you must also specify the operating conditions under boundary conditions. Fluent automatically sets the operating pressure to be atmospheric pressure. This can be adjusted to be zero as all pressures calculated will be absolute and not relative to a gauge pressure. For instance, absolute pressure is calculated by summing gauge pressure and operating pressure. If the latter is zero, then absolute pressure is equal to gauge pressure. This is required to be consistent with the pressure the ideal gas law and energy equations use. In addition, to obtain more realistic results as the scramjet is traveling at a high altitude, gravity can be considered. Per [37], at 26 km, the acceleration of gravity is approximately -9.727 meters per second squared in the y direction. Finally, Fluent recommends that for Mach numbers higher than 0.1, the specified operating density can be considered 0. The Boussineq temperature can be modified to be the static temperature. While gravity may not be a leading factor in the governing equations, it does act as a numerical stabilizer in CFD. Given that the CIAM/NASA Scramjet is also traveling at a high velocity where density is constantly changing, gravity needs to be defined as it preconditions pressure, activates buoyancy, and accounts for backflow more accurately.

3.2.5 Wall and Outlet Conditions

For simplicity, the wall conditions consider no-slip. In reality, the shear stress would be calculated for each segment of the scramjet and inputted into Fluent. Regarding the outlet, the type should be set to pressure outlet, where the gauge pressure value is set equal to zero.

3.2.6 Reference Values

The reference values are the values used in the post-processing step to calculate normalized flow-field variables. Since the scramjet being analyzed is traveling at Mach 6.5 at 26 km, using atmospheric values would not be accurate. Instead, Fluent allows the user to select an area whose boundary conditions have already been inputted to use as reference values, and calculates any necessary values based on the input. The reference values used in this project are those from the inlet.

3.2.7 Monitor Settings

Under the Monitor section in the menu, there is an option for Residuals. Residuals represent the difference in solution values between the previous iteration and the current iteration. There is a convergence criteria that is used to determine when the values can be said to have converged. The default value is 0.001. However, for this project the value was adjusted to be 1e-6, which is more commonly used for CFD.

3.2.8 Initialization

The subsequent step that follows the reference values is initialization. Since the goal is to replicate previous findings and the freestream conditions are known, standard initialization is selected. By selecting inlet for the area to compute the initialization from, all the parameters inputted before will appear.

3.2.9 Running Calculation

For an initial run, steady state flow is considered. This will allow the user to get a sense of how the flow behaves. Therefore, when running the calculations, only the number of iterations needs to be adjusted. To get more accurate results, a large number of iterations should be inputted. However, that is greatly dependent on the computational power available.

3.3 Computational Fluid Dynamics Fundamentals

3.3.1 Conservation Equations

Physical properties of a fluid flow derive from the fundamental principles of mass and energy conservation. As well as Newton's Second Law of Motion, which states the acceleration is proportional to the net force acting upon it. These principles are described by integrals or partial differential equations (PDEs). These equations are known as the Navier-Stokes Equations. One can begin with the equations for three-dimensional, unsteady flow from [38]. The first equation is the continuity equation, seen below:

$$\frac{\partial \rho}{\partial t} + \frac{\partial(\rho u)}{\partial x} + \frac{\partial(\rho v)}{\partial y} + \frac{\partial(\rho w)}{\partial z} = 0 \tag{3.1}$$

where ρ is the density, u is the x-component of velocity, v is the y-component of velocity, w is the z-component of velocity, and t is time. The continuity equation states that whatever mass is entering the system must be the same as the mass exiting the system.

Next, Newton's Second Law of Motion, or the conversation of momentum equations for the x, y, and z direction, respectively:

$$\frac{\partial(\rho u)}{\partial t} + \frac{\partial(\rho u^2)}{\partial x} + \frac{\partial(\rho uv)}{\partial y} + \frac{\partial(\rho uw)}{\partial z} = -\frac{\partial p}{\partial x} + \frac{1}{Re}\left[\frac{\partial \tau_{xx}}{\partial x} + \frac{\partial \tau_{xy}}{\partial y} + \frac{\partial \tau_{xz}}{\partial z}\right] \tag{3.2}$$

$$\frac{\partial(\rho v)}{\partial t} + \frac{\partial(\rho uv)}{\partial x} + \frac{\partial(\rho v^2)}{\partial y} + \frac{\partial(\rho vw)}{\partial z} = -\frac{\partial p}{\partial y} + \frac{1}{Re}\left[\frac{\partial \tau_{xy}}{\partial x} + \frac{\partial \tau_{yy}}{\partial y} + \frac{\partial \tau_{yz}}{\partial z}\right] \tag{3.3}$$

$$\frac{\partial(\rho w)}{\partial t} + \frac{\partial(\rho uw)}{\partial x} + \frac{\partial(\rho vw)}{\partial y} + \frac{\partial(\rho w^2)}{\partial z} = -\frac{\partial p}{\partial z} + \frac{1}{Re}\left[\frac{\partial \tau_{xz}}{\partial x} + \frac{\partial \tau_{yz}}{\partial y} + \frac{\partial \tau_{zz}}{\partial z}\right] \tag{3.4}$$

where p is the pressure, Re is the Reynolds Number, and τ is the stress tensor with the subscripts being the components of the tensor. The stress tensor is considered for the conservation of momentum as forces, such as normal force and shear force due to viscosity, are applied to the surfaces of the body. The tensor components can be described as the following [39]:

$$\tau_{xx} = -\frac{2}{3}\mu(\nabla \cdot \mathbf{V}) + 2\mu\frac{\partial u}{\partial x} \tag{3.5}$$

$$\tau_{yy} = -\frac{2}{3}\mu(\nabla \cdot \mathbf{V}) + 2\mu\frac{\partial v}{\partial x} \tag{3.6}$$

$$\tau_{zz} = -\frac{2}{3}\mu(\nabla \cdot \mathbf{V}) + 2\mu\frac{\partial w}{\partial x} \tag{3.7}$$

$$\tau_{xy} = \tau_{yx} = \mu\left(\frac{\partial v}{\partial x} + \frac{\partial u}{\partial y}\right) \tag{3.8}$$

$$\tau_{xz} = \tau_{zx} = \mu\left(\frac{\partial u}{\partial z} + \frac{\partial w}{\partial x}\right) \tag{3.9}$$

$$\tau_{yz} = \tau_{zy} = \mu\left(\frac{\partial w}{\partial y} + \frac{\partial v}{\partial z}\right) \quad (3.10)$$

where μ is the viscosity and $\nabla \cdot \mathbf{V}$ is the divergence of the velocity field. The second term comes from the symmetric velocity gradient tensor. The divergence contributes to the surface-force terms for the momentum. It is important to consider the shear force as the force itself creates the boundary layers at the surface of the body, which in turn induces friction drag. In addition, the interaction the shear force at the wall has with the pressure forces determines how much boundary layer separation there will be and the losses that result from that separation. Finally, considering the shear force implies that the shear layers that are between the incoming streams will assist with mixing the fuel with air and thus, improving the mixing rate [39].

The last is the conservation of energy equation, described as:

$$\frac{\partial(E_t)}{\partial t} + \frac{\partial(uE_t)}{\partial x} + \frac{\partial(vE_t)}{\partial y} + \frac{\partial(wE_t)}{\partial z} = -\frac{\partial(up)}{\partial x} - \frac{\partial(vp)}{\partial y} - \frac{\partial(wp)}{\partial z} - \frac{1}{RePr}\left[\frac{\partial q_x}{\partial x} + \frac{\partial q_y}{\partial y} + \frac{\partial q_z}{\partial z}\right]$$
$$+ \frac{1}{Re}\left[\frac{\partial}{\partial x}(u\tau_{xx} + v\tau_{xy} + \tau_{xz}) + \frac{\partial}{\partial y}(u\tau_{xy} + v\tau_{yy} + w\tau_{yz}) + \frac{\partial}{\partial z}(u\tau_{xz} + v\tau_{yz} + w\tau_{zz})\right] \quad (3.11)$$

where E_t is the total energy, Pr is the Prandtl Number, and q is the heat flux.

Attempting to solve the Navier-Stokes equations via calculus would be extremely time-consuming. Thus, CFD software is used to accelerate the process, especially as more realistic flows are considered. CFD software uses the discretized domain specified by the user, which is typically the mesh and its elements. It converts the PDEs described above into linearized algebraic equations at each element and then solves those discretized algebraic forms [39]. The software uses a solver to find approximate solutions to the equations. This process is known as the finite volume method, which is what Fluent uses as its solver.

The exact variation of the energy equation that solvers consider varies from software to software. Fluent uses the variation below [40]:

$$\frac{\partial}{\partial t}(\rho E) + \nabla \cdot (\mathbf{V}(\rho E + p)) = \nabla \cdot \left(k_{eff}\nabla T - \sum_j h_j \mathbf{J}_j + \left(\tau_{ij} \cdot \mathbf{V}\right)\right) + S_h \quad (3.12)$$

where E is the total energy, k_{eff} is the effective conductivity, $\mathbf{J}_j$ is the diffusion flux of species j, and S_h contains the heat of chemical reaction and any other volumetric heat sources. One of the models mentioned in Section 3.2 was the energy equation. As the CIAM/NASA scramjet is traveling at Mach 6.5, temperature is varying on the surface. Thus, when the solver is attempting to solve the other equations, the value of temperature varies depending on the location, i.e. the element the solver is at. Solving the energy equation obtains the temperature field.

3.3.2 Turbulence Model

Fluid flow typically begins as a smooth laminar flow. Laminar flow is when the particles within the flow are moving parallel with respect to each other. It typically occurs at a low Reynolds number, where the viscous forces dominate the inertial forces and velocity is relatively constant. Nevertheless, flows realistically do not maintain a constant velocity and natural instabilities will form. Smooth behavior transitions into chaotic behavior, thus entering turbulent flow [41].

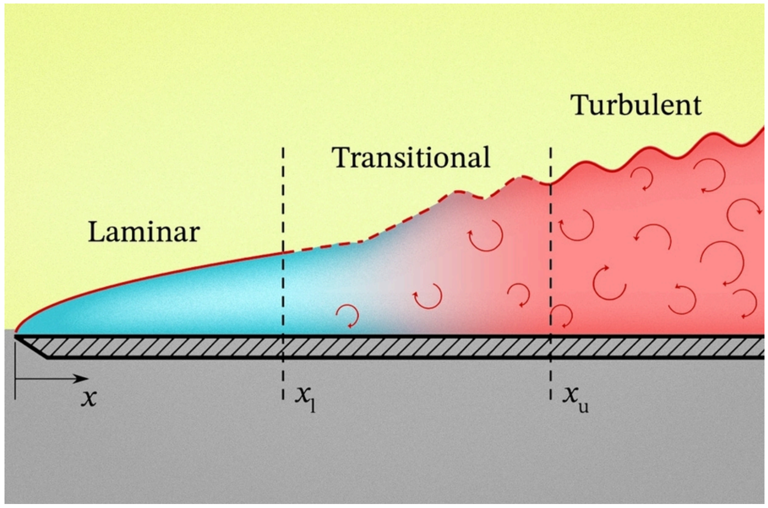

Figure 3.4 - Laminar-Turbulent flow transition [42]

Figure 3.4 depicts said transition. The flow becomes completely turbulent after a certain length. This is in line with the definition of Reynolds number, which is:

$$Re = \frac{\rho u L}{\mu} \tag{3.13}$$

where u is the velocity magnitude and L is the characteristic length. Thus, as the velocity and length increase, turbulent flow will occur at larger Reynolds numbers. Physically, there is enough kinetic energy to transition any existing instabilities into perpendicular flow movement, i.e. inertial forces are overcoming viscous forces. The result is an uneven pattern of swirls, as seen in **Figure 3.4**, also known as eddies. Moreover, eddies are physical representations of fluctuations within the flow. The velocity and pressure are constantly changing in both magnitude and direction [41,43].

Complications arise as the scale of the eddies forming is a spiraling effect. Large eddies will form smaller eddies, and those small eddies will form smaller eddies. Eventually, the miniscule eddies will release their translational and rotational energy as heat by shear forces. Unfortunately, engineers and physicists have had a complex time trying to find mathematical representations for turbulence flow due to its chaotic and unsteady nature. Understanding and attempting to model turbulent flow is important as it allows engineers to replicate aircraft conditions. By doing so, performance parameters, such as combustion, aerodynamics, heat transfer, and fluid structure interactions, can be optimized. [41,43]

A common method in CFD softwares to analyze turbulent flows is utilizing the Reynolds-averaged Navier-Stokes (RANS) equations. As mentioned before, turbulent flows have large scales of fluctuations. Therefore, it is more ideal to approach turbulence from a statistical point of view and consider averages and probability distributions [41,43]. Consider a time-dependent variable, such as velocity, and decompose it into its mean and fluctuation values, respectively, as such [43]:

$$\mathbf{V}(x,t) \;=\; \overline{\mathbf{V}}(x) + \mathbf{V}'(x,t) \tag{3.14}$$

which can be further simplified into its components: $u = \overline{u} + u'$, $v = \overline{v} + v'$, $w = \overline{w} + w'$. **Figure 3.5** provides an excellent representation of the new statistical values.

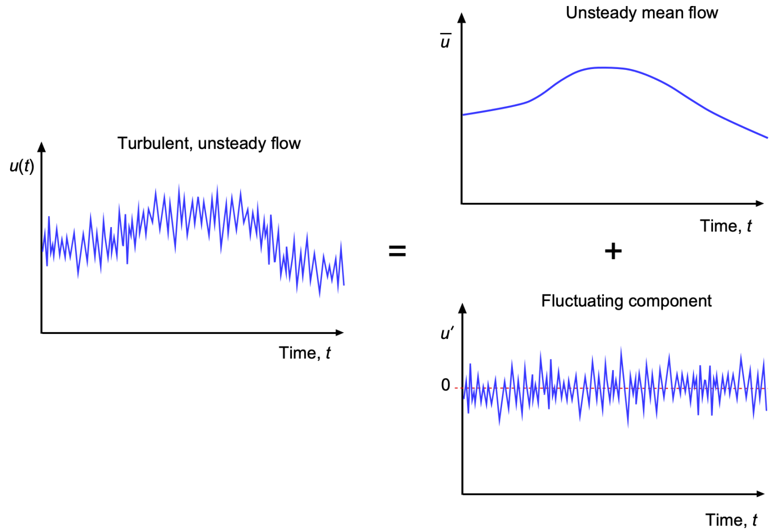

Figure 3.5 - Statistical decomposition of velocity component [43]

Eq. 14 can be substituted into Eq. 1-4, which results in the governing RANS equations used by CFD software. It is the averaging that reduces computing power by adding a few extra terms to the Navier-Stokes equations rather than attempting to derive and solve more complex equations.

In converting the Navier-Stokes equations into RANS equations, a new term is introduced: the Reynolds stress tensor. There are more unknowns to solve than there are equations. To address this issue, models are introduced to assist in solving the Reynolds stress tensor [43]. Fluent offers many models to choose from. However for this project, the Shear Stress Transport (SST) k-ω turbulence model was chosen. It supplies RANS equations with robust predictions in extreme pressure gradient boundary layer regions, as well as shock-boundary layer interactions. This is particularly ideal for cases that involve scramjet inlets.

The SST k-ω turbulence model is a two equation model. The two equations being two transport equations: turbulence kinetic energy, k, and specific dissipation rate, ω. It was developed by Menter, who aimed to combine the accuracy and robustness of the standard k-ω model near the surface wall with the free-stream effects away from the surface that the k-ϵ model offers. Combining both models reduces the free-stream sensitivity whilst maintaining accurate low Reynolds number convergence. It also provides a limit for turbulent shear stress to avoid over estimating any flow separation [44]. The two transport equations that Fluent uses are [44]:

$$\frac{\partial}{\partial t}(\rho k) + \frac{\partial}{\partial x_i}\left(\rho k u_i\right) = \frac{\partial}{\partial x_j}\left(\Gamma_k \frac{\partial k}{\partial x_j}\right) + \overline{G_k} - Y_k + S_k \tag{3.15}$$

$$\frac{\partial}{\partial t}(\rho \omega) + \frac{\partial}{\partial x_i}(\rho k \omega) = \frac{\partial}{\partial x_j}\left(\Gamma_\omega \frac{\partial \omega}{\partial x_j}\right) + G_\omega - Y_\omega + S_\omega + D_\omega \tag{3.16}$$

where $\overline{G_k}$ is the turbulence kinetic energy that the mean velocity gradients generate, G_{ω} is the generation of the specific dissipation rate, Γ_k and Γ_{ω} are the effective diffusivity of k and ω, respectively, Y_k and Y_{ω} are the dissipation rate generated by turbulence of k and ω, respectively, S_k and S_{ω} are user-defined terms, and D_{ω} is the cross-diffusion term.

3.4 Results and Comparison

After running 1000 iterations, **Figure 3.6**, **Figure 3.7**, and **Figure 3.8** were produced.

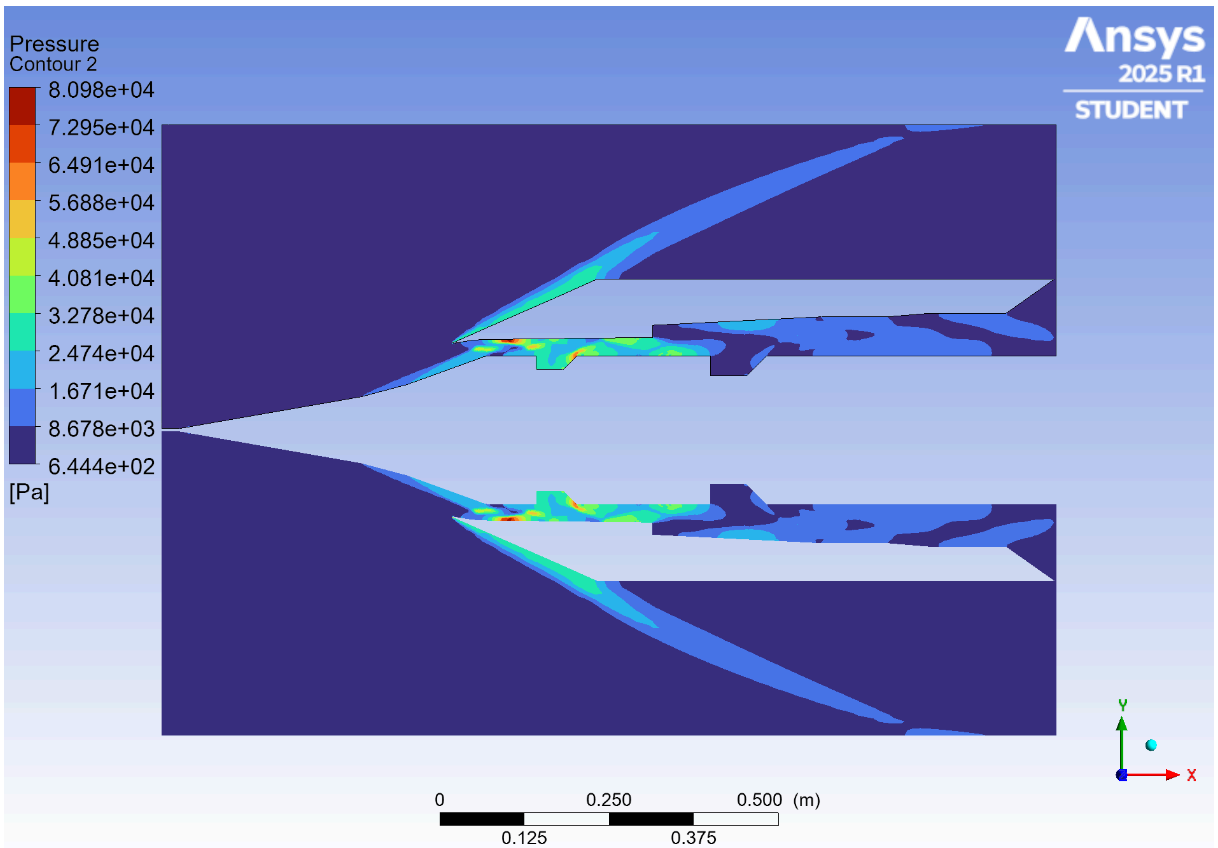

Figure 3.6 - Static pressure contour

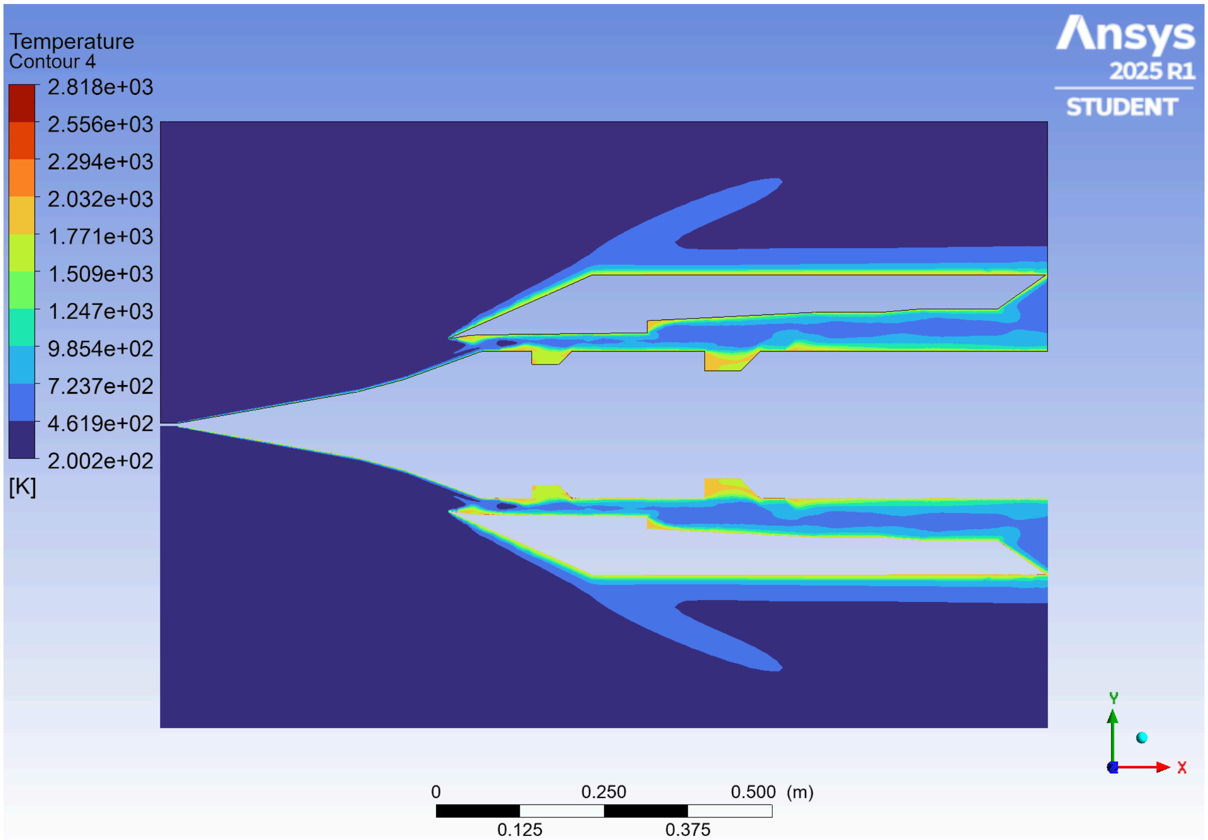

Figure 3.7 - Static temperature contour

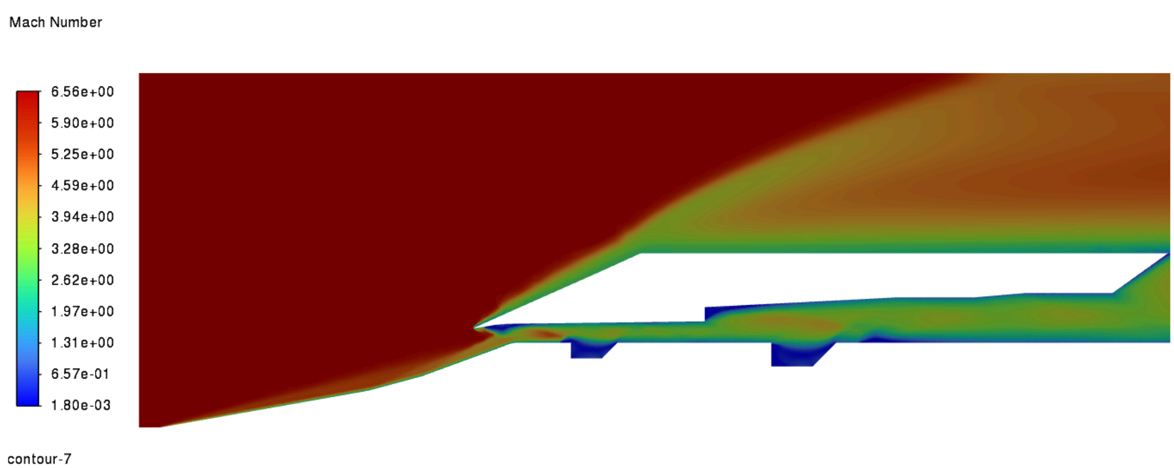

Figure 3.8 - Mach number contour

For verification purposes, only the inlet will be considered, which will be defined by the start of the isolator. In **Figure 3.6**, the static pressure at the inlet is approximately 43,500 Pa. McClinton et. al [34] states that NASA predicted an inlet static pressure of 40,000 Pa and CIAM predicted an inlet static pressure of 39,000 Pa. In **Figure 3.7**, the static temperature at the inlet is 630 K. McClinton et. al [34] states that NASA predicted an inlet static temperature of 651 K. In **Figure 3.8**, the Mach number at the inlet is approximately 3.5. McClinton et. al [34] states that

NASA predicted an inlet Mach number of 3.2 and CIAM predicted an inlet Mach Number of 3.15.

The contour plots produced by the geometry, mesh, and parameter setup described above provide values within bounds to those that NASA and CIAM predicted for the axisymmetric dual-mode scramjet. The exact same values cannot be reproduced as some components of the geometry had to be calculated based on existing measurements, thus not having the exact measurements as the CIAM/NASA scramjet. In addition, the exact shear stress conditions at the wall were not considered in this verification process. The meshing could have also been more fine. Despite the simplifications, the scramjet design from **Figure 2.12** has inlet conditions that are well within limits of published data from [34] and further analysis can be continued.

4. Scramjet Theoretical Verification

4.1 Oblique Shockwaves

When supersonic flow travels into a wall deflected upward by some angle, θ, an oblique shock wave will form, as seen in **Figure 4.1**.

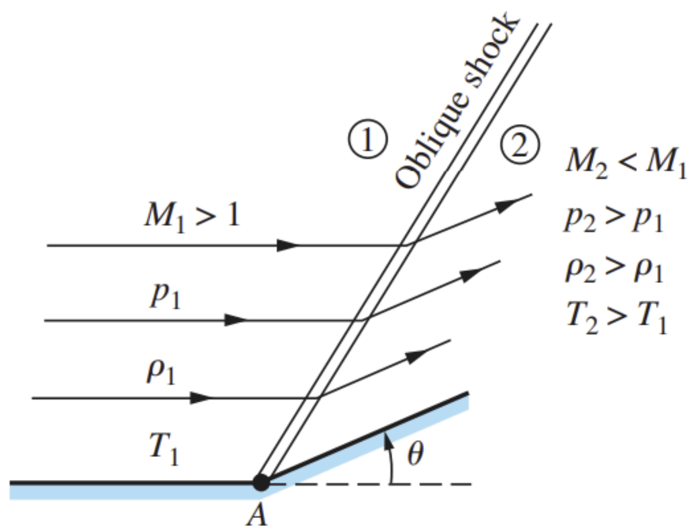

Figure 4.1 - Oblique shock wave properties [28]

A common conception about oblique shock waves is that the flow is turning in on itself due to the deflection of the surface, or in the case of **Figure 4.1**, the wall. As a result, the streamlines after the shockwave are then deflected at the same angle, θ, following the path of the main part of the incoming flow [28]. In addition, the flow will decelerate across the oblique shock wave, thus resulting in a decrease in Mach number and an increase in density, pressure and temperature.

However, oblique shock waves have many more properties than displayed in **Figure 4.1**. There are two angles to consider, one being the deflection angle, θ, and the other being the wave angle, β. The wave angle, β, displayed in **Figure 4.2**, is defined by the angle between the base of the deflection angle and the shock wave. Therefore, the distance between the shock wave and the wall can be denoted by $\beta - \theta$.

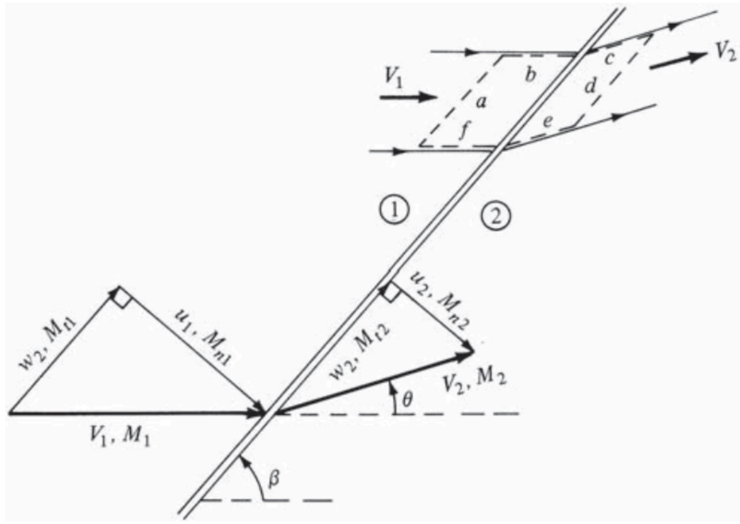

Figure 4.2 - Oblique shock wave properties and geometry [28]

Furthermore, as a result of the flow being deflected upward, breaking the Mach number down into components allows for better analysis moving forward. The upstream Mach number is composed of a normal component, denoted by M_{n1}, and a tangential component, denoted by M_{t1}. The downstream Mach number is also composed of a normal component, denoted by M_{n2}, and a tangential component, denoted by M_{t2}. The same logic can be applied to the velocity upstream and downstream the shockwave, where they are denoted by normal and tangential components u_1, w_1 and u_2, w_2, respectively [28].

To understand how the velocity components differ across the shock wave, consider the continuity equation assuming steady state, constant area in control volume, incompressible, adiabatic flow with no external forces below:

$$\oiint \rho \mathbf{V} \cdot \mathbf{ds} = 0 \tag{4.1}$$

where ρ is the density and V is the velocity vector. The only faces that make a contribution to Eq. 4.1 from Fig. 4.1 are a and d which simplify Eq. 4.1 to:

$$\rho_1 u_1 = \rho_2 u_2 \tag{4.2}$$

where ρ_1 is the density upstream and ρ_2 is the density downstream.

Next, conservation of momentum can be considered as seen below:

$$\frac{\partial}{\partial t} \oiiint \rho \mathbf{V}\, d\mathcal{V} + \oiint (\rho \mathbf{V} \cdot \mathbf{ds})\mathbf{V} = -\oiint p\, \mathbf{ds} + \oiiint \rho \mathbf{f}\, d\mathcal{V} + \mathbf{F}_{viscous} \tag{4.3}$$

where $\mathcal{V}$ is control volume, p is the pressure, f is the net body force, and $F_{viscous}$ is the viscous force. Fortunately, considering the same assumptions as was done for the continuity equation and the fact that it is a vector equation, Eq. 4.3 can be represented by its normal and tangential components described below:

$$\oiint(\rho\mathbf{V}\cdot\mathbf{ds})u = -(\oiint p\,ds)_{normal} \tag{4.4}$$

$$\oiint(\rho\mathbf{V}\cdot\mathbf{ds})w = -(\oiint p\,ds)_{tangential} \tag{4.5}$$

which can be simplified to the following equations, respectively:

$$p_1 + \rho_1 u_1^2 = p_2 + \rho_2 u_2^2 \tag{4.6}$$

$$w_1 = w_2 \tag{4.7}$$

where the subscript 1 denotes an upstream condition and the subscript 2 denotes a downstream condition.

The last conservation equation to consider is the conservation of energy denoted below:

$$\oiiint\dot{q}\rho\,d\dot{q}\mathcal{V} + \frac{dQ}{dt}_{viscous} - \oiint\rho\mathbf{V}\cdot\mathbf{ds} + \oiiint\rho(\mathbf{f}\cdot\mathbf{V})\,d\mathcal{V} + \dot{W}_{viscous}$$

$$= \frac{\partial}{\partial t}\oiiint\rho(e + \frac{V^2}{2})\,d\mathcal{V} + \oiint\rho(e + \frac{V^2}{2})\mathbf{V}\cdot\mathbf{ds} \tag{4.8}$$

where dQ/dt is the rate of heat addition due to viscous effects to the control volume, $\dot{W}_{viscous}$ is the rate of work done due to viscous effects to the control volume, and e is the internal energy. Considering the same assumptions as before, Eq. 4.8 simplifies to:

$$\oiint\rho(e + \frac{V^2}{2})\mathbf{V}\cdot\mathbf{ds} = -\oiint\rho\mathbf{V}\cdot\mathbf{ds} \tag{4.9}$$

Solving Eq. 4.9 results in the following:

$$h_1 + \frac{V_1^2}{2} = h_2 + \frac{V_2^2}{2} \tag{4.10}$$

where h_1 and h_2 is the enthalpy upstream and downstream, respectively. However, if V were to be split into its normal and tangential components and knowing Eq. 4.7, Eq. 4.10 further simplifies to:

$$h_1 + \frac{u_1^2}{2} = h_2 + \frac{u_2^2}{2} \tag{4.11}$$

To recap, from the conservation of mass, momentum, and energy, Eq. 4.2, Eq. 4.6, and Eq. 4.11 are obtained. These are the results of the simplified case compared to the conservation equations mentioned in Section 3.2, which are universal. Common across all three equations is that the tangential velocity is not included. It can then be assumed that the tangential velocity is not influential on the oblique shock wave properties and only the normal component of the velocity can be considered.

The velocity relations for oblique shock waves have been identified. Then precedes the Mach number relations. As mentioned before, the Mach number has normal and tangential components as well. The normal component of Mach number is the only component considered as seen in the relationship below:

$$M_{n,1} = M_1 sin\beta \tag{4.12}$$

Once $M_{n,1}$ is known, the oblique shock wave can be treated as a normal shock wave which results in the following equations:

$$M_{n,2}^2 = \frac{1+[(\gamma-1)/2]M_{n,1}^2}{\gamma M_{n,1}^2-(\gamma-1)/2} \tag{4.13}$$

$$\frac{\rho_2}{\rho_1} = \frac{(\gamma+1)M_{n,1}^2}{2+(\gamma-1)M_{n,1}^2} \tag{4.14}$$

$$\frac{p_2}{p_1} = 1 + \frac{2\gamma}{\gamma+1}(M_{n,1}^2 - 1) \tag{4.15}$$

$$\frac{T_2}{T_1} = \frac{p_2}{p_1}\frac{\rho_1}{\rho_2} \tag{4.16}$$

where Eq. 4.13 is used to find the downstream normal Mach number, Eq. 4.14 is the density ratio, Eq. 4.15 is the pressure ratio, and Eq. 4.16 is the temperature ratio. Thus, upstream and downstream conditions can be found for an oblique shock wave.

While Eq. 4.13 gives the normal Mach number, which corresponds to a normal shock wave; it has to be translated into the oblique shock wave Mach number. This can be done by using the equation below:

$$M_2 = \frac{M_{n,2}}{sin(\beta-\theta)} \tag{4.17}$$

The final oblique shock wave relation that relates M_1 and β, the main independent variables, with the secondary variable, θ, is the following:

$$tan\,\theta \;=\; 2\,cot\,\beta\frac{M_1^2 sin^2\beta-1}{M_1^2(\gamma+cos\,2\beta)+2} \tag{4.18}$$

which is also known as the $\theta - \beta - M$ relation. Attempting to solve it analytically is quite difficult, so it it typically plotted for a variety of β, θ, and M values for one specific heat ratio [28].

4.2 Scramjet Wave Analysis and Comparison

This section will utilize Eq. 4.12, Eq. 4.13, Eq. 4.15, Eq. 4.16, and Eq. 4.17 to calculate the corresponding values for the CIAM/NASA Scramjet inlet, as seen in section A of **Figure 2.12**. The same assumptions used to derive the equations will be used for the chosen scramjet.

The values obtained by CIAM and NASA were obtained using a variety of numerical methods. For the CIAM predicted values, the external and internal inlet, i.e. the compression ramp and the section of the inlet right before the isolator, were calculated using an in house RANS solver. The solver utilized a second order implicit Godunav, a Baldwin-Lomax turbulence model, assumed a blunt centerbody and sharp cowl, and considered the plane to be axisymmetric. Regarding the values NASA predicted, the external and internal inlet were calculated using GASP. GASP is a two-dimensional and three-dimensional full Navier-Stokes solver. It considered finite-rate chemical kinetics, the Baldwin-Lomax turbulence model, and the k-ε turbulence model for combustion modeling.

The inlet ramp consists of three different angles, 10°, 15°, and 20°, respectively. The first oblique shock wave will occur at the 10° ramp. The freestream Mach number is 6.5.

Table 4.1 - First Oblique Shock Wave

Parameter	**Value**
M_1	6.5
β	16.92°
θ	10°
P_2/P_1	4.0129
T_2/T_1	1.6022
P_2	8,680.06 Pa
T_2	356.57 K
M_2	4.948

Now, the output values from the first oblique shock wave will be used as input parameters for the second oblique shock wave at the second ramp of 15°. However, since we are considering the change in angle from the previous ramp, the turn angle is considered to be 5°.

Table 4.2 - Second Oblique Shock Wave

Parameter	Value
M_2	4.9486
β	15.19°
θ	5°
P_3/P_2	1.7957
T_3/T_2	1.1889
P_3	15,586.78 Pa
T_3	423.92 K
M_3	4.45

The output values from the second oblique shock wave will be used as input parameters for the third oblique shock wave at the third ramp of 20°. As before, the change in angle from the previous ramp is considered. Therefore, the turn angle is 5° as well.

Table 4.3 - Third Oblique Shock Wave

Parameter	Value
M_3	4.45
β	16.5°
θ	5°
P_4/P_3	1.7011
T_4/T_3	1.169
P_4	26,514.67 Pa
T_4	495.56 K
M_4	4.02

The values in Table 4.3 would correspond to the area right before the tip of the cowl. Considering the inlet performance results from [34], the results obtained in Section 3, and the oblique shock wave values, there is quite the discrepancy between the first two methods and the latter. This is mainly due to how NASA and CIAM considered where the inlet starts.

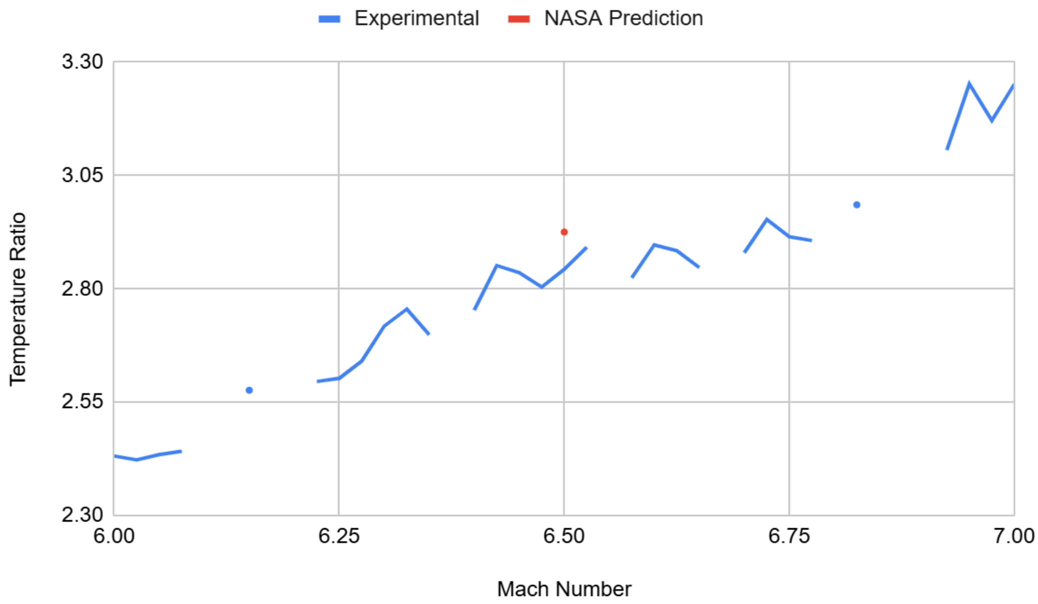

Figure 4.3 - Temperature ratio as a function of mach number for inlet exit

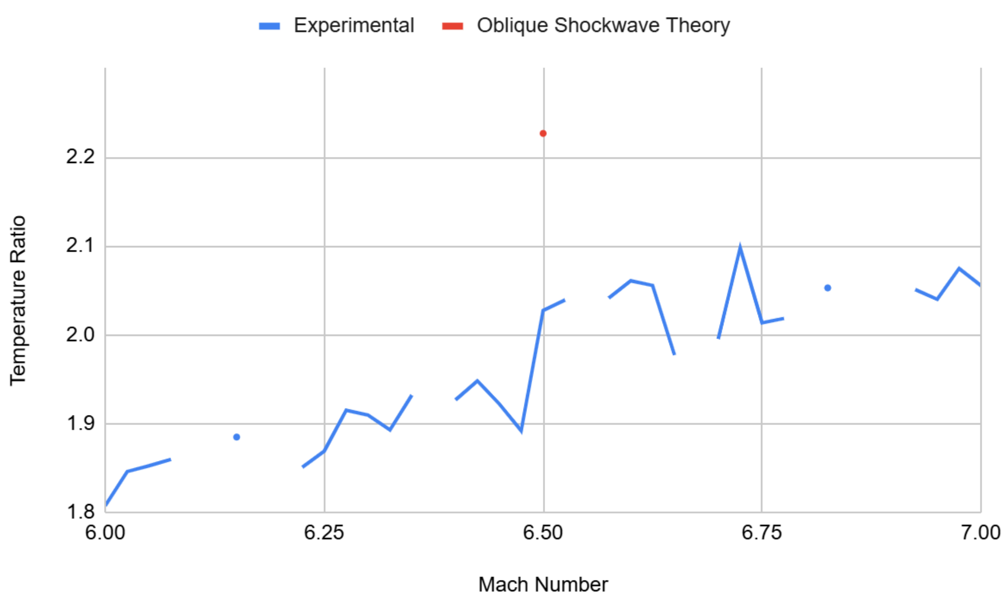

Figure 4.4 - Temperature ratio as a function of mach number for inlet entrance

The main difference between **Figure 4.3** and **Figure 4.4** is where the inlet temperature was calculated. The temperature ratio is defined as the inlet temperature divided by the initial static temperature. **Figure 4.3** had the inlet temperature calculated right before the isolator starts. **Figure 4.4** has the inlet temperature calculated right before the cowl tip. A difference in inlet temperature values is expected as the fluid before the cowl tip went through three oblique shock waves and the fluid before the isolator goes through oblique shock waves and expansion waves.

In **Figure 4.3**, the temperature ratio using the inlet temperature NASA predicted is depicted in red. It is relatively close to the temperature ratio calculated by using CFD. As mentioned before, obtaining the exact value would not be feasible as the geometries are not the exact same and the CFD set up would differ. In **Figure 4.4**, the temperature ratio using the temperature calculated after the third oblique shock wave is depicted in red. There is a larger difference between oblique shock wave physics and what CFD calculated compared to that in **Figure 4.3**. However, it is still within reason as oblique shock waves consider many assumptions about the flow and CFD can account for more complex physics.

Overall, there is an increasing trend in the temperature ratio as the Mach number increases. This aligns with the physics of shock waves. The kinetic energy of the flow is transferred to thermal energy as a result of the sudden compression of the flow. As the flow travels faster, the compression is stronger and thus creating a larger difference in temperatures. Interestingly, the gaps in both **Figure 4.3** and **Figure 4.4** are a consequence of the CFD simulations. For some Mach numbers, the solutions would not converge. This would produce values that were not physically possible. The mesh set up in Section 3 is relatively simple. This has an effect on the CFD simulations as it is trying to replicate complex physics, yet the location the software is attempting to solve the equation is not as clear as it could be. Fortunately, this issue only occurred for some Mach numbers, and there was enough data to graph the temperature ratios.

5. Fuel Injection Integration

5.1 CAD Modifications for Fuel Injectors

Per **Figure 2.11**, the location of the fuel injectors is on the annular duct. If a realistic simulation is desired, then the previous 2D CAD model of the CIAM/NASA scramjet would have to be converted to 3D. This would put all 42 fuel injectors for station 1, 2, and 3 in their rightful locations. However, to save computational time, only the diameter of a fuel injector is considered and inserted as a slot into the 2D CAD model.

To further simplify the geometry, Rodriguez [45] found, through communication with the authors from [35], that the first fuel injector station did not open as a result of possible large flow separation in the inlet of the actual flight test. Rodriguez [45] also found that computing CFD simulations would be easier by solving the inlet and combustion chamber separately, yet in order, as a result of the fuel injectors staying shut at station 1. For the remainder of this project, the CFD simulation will center around the combustion chamber, thus only the combustion chamber geometry will be considered. **Figure 5.1** and **Figure 5.2** displays the updated geometry for the fuel injector at station 2 and station 3, respectively. These values were taken from Rodriguez [45].

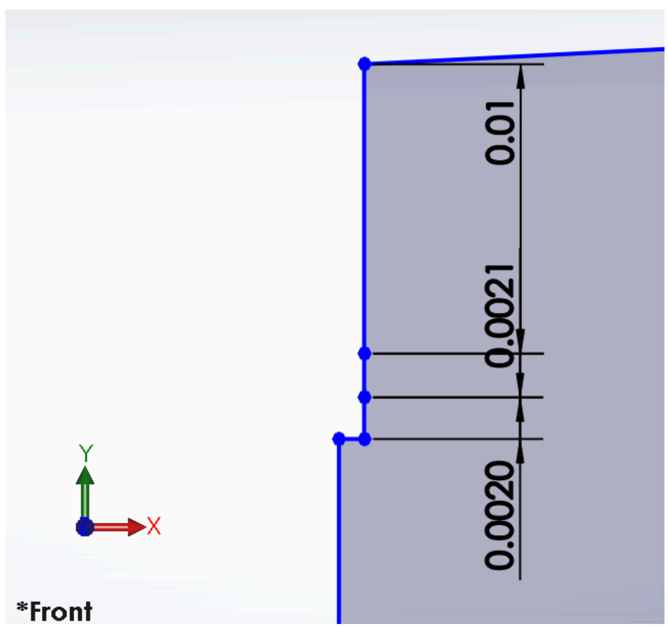

Figure 5.1 - Fuel injector dimensions at station 2

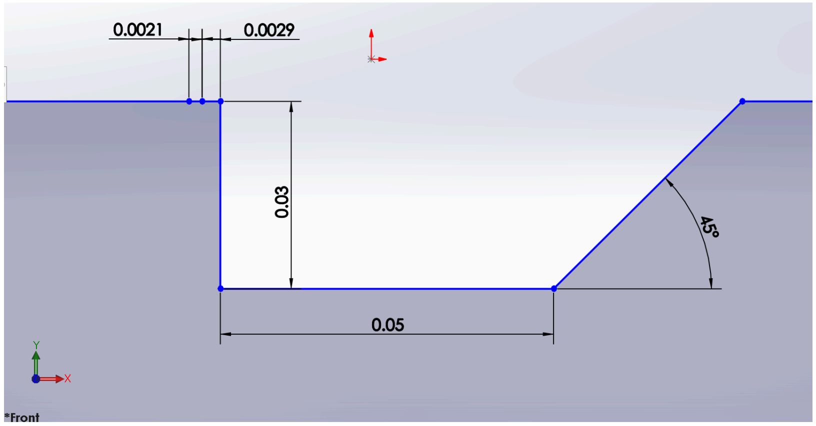

Figure 5.2 - Fuel injector dimensions at station 3

The combustion chamber begins slightly upstream from station 2, as seen in **Figure 5.3**, and the rest of the geometry remains the same as **Figure 2.12**.

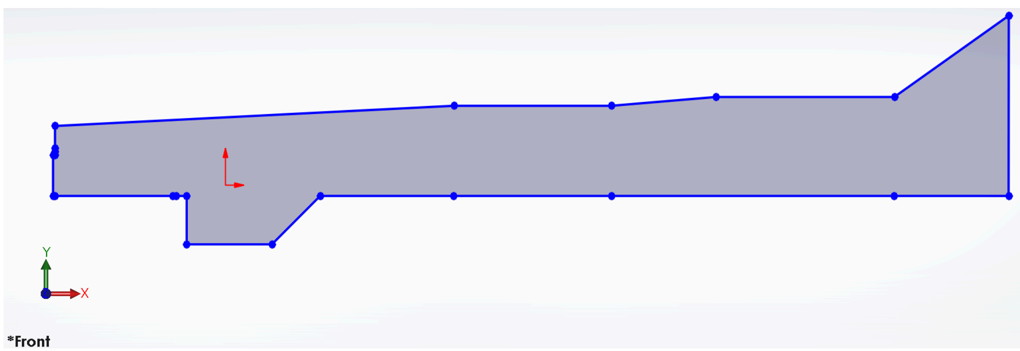

Figure 5.3 - Combustion chamber geometry with fuel injectors

Similar steps from Section 3 are applied to **Figure 5.3**, where the enclosed sketch was converted to a solid surface via the Planar Surface tool in Solidworks. Thus, the combustion chamber geometry that will be used for the CFD simulation in Fluent can be seen in **Figure 3.1**. In this case, there is no need to create a rectangular surface and then cut out the outline of the chamber as before. The desired physics occurs within the geometry rather than the surrounding.

Figure 5.4 - Combustion chamber surface

5.2 Combustion Chamber Boundary Conditions

The premise of Rodriguez [45] was to conduct CFD analysis of the CIAM/NASA scramjet to determine if the flight test data could be replicated and understood. Beginning with the inlet analysis, the CFD results were compared to the data. Rodriguez [45] concluded that the CFD was not displaying the major flow separation to the extent that is known to have occurred. The wall pressure via CFD decreased shortly after the internal inlet, whereas the flight data found that the wall pressure continued to increase as it traveled into the inlet. At the exit of the inlet, i.e. the entrance of the combustion chamber, the known Mach number was Mach 2 from flight data after the scramjet was fired for 56 seconds. Yet, the CFD results found the Mach number to be 2.67. Rodriguez [45] also attempted to run the simulation in time intervals rather than one entire interval. While it was determined that there was some improvement in the wall pressure values, as well as the Mach number being 2.4, it was still not close enough to completely agree with the flight data. Overall, the patterns are similar in the CFD results and the data as in the time intervals of 25 seconds and 38 seconds, there is boundary layer separation preventing the inlet from starting. At the 56 seconds mark, the inlet has started, but the flow is still separated and is slowly starting to recirculate.

It is this discrepancy in data that Rodriguez [45] determined for the combustion chamber entrance conditions should replicate what occurred in the flight data, and not follow what the CFD results state. The equivalence ratio, mass flowrate, total temperature, and turbulence conditions, combustion chamber entrance Mach number from the flight test data and 1D analysis were utilized to calculate uniform combustion chamber entrance conditions. The values can be found in Table 5.1.

Table 5.1 - Combustion Chamber Entrance Conditions [45]

Parameter	Value
T_0	1632 K
ρ	0.467 kg/m^3
M	2.0
τ_{int}	0.06
μ_T/μ_L	350

5.3 Fuel Injector Boundary Conditions

Hydrogen fuel was injected in application, and is therefore being carried in the CFD analysis as well. The injection values utilized in Rodriguez [45] can be found in Table 5.2.

Table 5.2 - Fuel Injector Conditions

Parameter	**Station 2**	**Station 3**
M	1.0	1.0
T_0 [K]	716	771
T [K]	597	642
U [m/s]	1864	1934
ρ $[kg/m^3]$	0.155	0.149
W [kg/s]	0.042	0.042

5.4 Updated Mesh

Following the same principle at Section 3.1.2, a fine mesh is also required in this step of the project. However, since the geometry was simplified significantly compared to **Figure 3.3**, the mesh does not require as much computational time to generate. Inserting face sizing with elements of 1 millimeter and inflation on all the walls with layers of 10, **Figure 5.5** would be sufficient to analyze the turbulent flow, specifically the shear layer and shock interactions occurring near the wall.

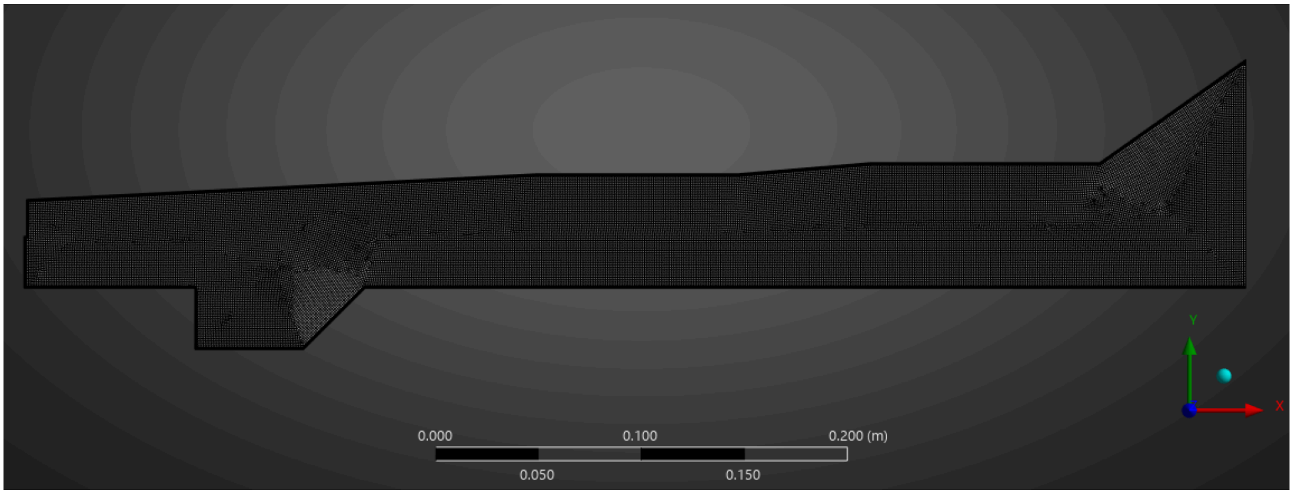

Figure 5.5 - Combustion Chamber Mesh

Detailed information regarding overall mesh information can be found in Table 5.3.

Table 5.3 - Combustion Chamber Mesh Information

Parameter	Value
Growth Rate	1.2
Transition Ratio	0.272
Target Skewness	0.9
Orthogonal Quality	> 0.21583
Max Aspect Ratio	3.332
Nodes	48,530
Elements	47,853

The geometry also has to be named while in Mechanical to allow Fluent to automatically detect the boundary types. The inlet is specified to be the vertical line before the small step. The injectors are names based on their locations, which are defined in **Figure 5.1** and **Figure 5.2**. The outlet is specified to be the vertical line on the right end of the combustion chamber. Everything else is specified to be a wall.

5.5 Updated Simulation Set Up

5.5.1 General Task Page

As in Section 3.2.1, a density-based solver is chosen. Instead of assuming the solver time to be steady, it is changed to transient. This is mandatory as the physics that occurs within the scramjet is time-dependent. First and foremost, it is important to know when and where the fuel-air mixture first ignites. Time is also a factor in the chemistry as there are reaction times to consider for the given time a scramjet has for operation. Additionally, how the flame will develop, move, and stabilize as it moves across the combustion chamber must be considered. Until the flame stabilizes, parameters such as pressure, temperature, and the mass fraction of the species, will vary with time. Furthermore, as a result of airflow entering at Mach 2 and fuel injection occurring at Mach 1, there are shock-shear layer interactions. These interactions are not static. The intensity and location also vary in time. Thus, to accurately capture the effects of shock-shear layers with ignition, time must be included.

5.5.2 Model Selection

The energy equation is selected again. To begin the simulations, the realizable k-ε viscous model with standard wall functions is selected. All default parameters remain unchanged. It allows for a solid foundation that can then be built upon by transitioning to a more strict model that can handle the intensity of physics occurring near the wall. As fuel injection is now being implemented, the species model is turned on. Volumetric reactions are selected as well as the reactions occurring between the gas and the working fluid occurring within the fluid volume add a chemical source term to the species and energy equations. The mixture material chosen is hydrogen-air, which for the first iteration of this project, is left as the default settings. There will be a total of 4 species considered in the reaction mechanism Fluent implements. Regarding the Turbulence-Chemistry interaction, Finite-Rate/Eddy-Dissipation is chosen. Computationally, it is the more robust option out of the rest. Physically, it is the best option as the combustion chamber operates in a regime where chemical kinetics and turbulent mixing can alternate in which takes precedence in the overall reaction rate. In low-temperature regions, or where ignition is low, the finite-rate chemistry limits the reaction rate. When transitioning to flame and shear-layer regions, the process transfers from finite-rate chemistry to becoming mixing-controlled. Finite-Rate/Eddy-Dissipation determined which to use by calculating both the Arrhenius finite-rate and the turbulence-based eddy-dissipation rate in each cell. It then adopts the smaller value that results in the most effective reaction rate.

5.5.3 Material Selection

In the Material Selection tab, there are now three options: fluid, solid, and mixture. Now that fuel injection is being studied, the fluid domain will consist of the mixture only. Therefore, for the hydrogen-air mixture, the density and viscosity is changed from the default setting to ideal-gas and Sutherlands, respectively.

5.5.4 Cell Zone and Boundary Conditions

Fluent should automatically select the hydrogen-air mixture as the material for the fluid zone under the Cell Zone Conditions.

The airflow inlet boundary conditions used are those mentioned in Table 5.1. However, regardless of the boundary type selected for the airflow inlet, a pressure needs to be inputted. Velocity-inlet is the chosen, and it will require the static temperature, static pressure, and the velocity magnitude to be calculated. Using ideal-gas relations, the following equations are utilized:

$$T = \frac{T_o}{1+\frac{\gamma-1}{2}M^2} \tag{5.1}$$

$$P = \rho RT \tag{5.2}$$

$$M = \frac{V}{a} \tag{5.3}$$

$$a = \sqrt{\gamma RT} \tag{5.4}$$

For Eq. 5.1 and Eq. 5.2, ideal air is considered. Thus, gamma is 1.4 and R, the specific gas constant, is 287 J/(kg·K). The static temperature, static pressure, and velocity calculated are 907 K, 122,000 Pa, and 1,207 m/s, respectively. For Fluent, static pressure is inputted for supersonic/initial gauge pressure. The outflow gauge pressure can be left as zero. As for the species mass fractions, there is 0.232 of O_2 and 0.032 of H_2O. The turbulence specification model chosen is intensity and length method as Fluent recommends it for wall-bounded flows where there are turbulent boundary layers. The intensity is left as the default value. The length is

The fuel injector boundary conditions used are those mentioned in Table 5.2. They are also considered to be velocity-inlets. For the supersonic/initial gauge pressure, the same pressure utilized for the airflow inlet can be used for both injectors. Per McClinton et al. [34], the second injector is at 30 degrees and the third injector is at 45 degrees. To account for the x- and y-components for the direction trigonometry is considered. Table 5.3 established the components for both injectors.

Table 5.4 - Fuel Injector Direction

Direction	**Station 2**	**Station 3**
X-component	0.5	0.707
Y-component	-0.866	0.707

For the species mass fraction for both fuel injectors, the mass consists entirely of liquid hydrogen, thus being 1. The turbulence specification method used is the same as the airflow inlet, as well as the parameters.

5.5.5 Wall and Outlet Conditions

As Section 3.2.5, the no-slip condition is applied to the wall for simplicity and to reduce computational time. The outlet boundary type is selected to pressure-outlet, and the values are left unchanged.

5.5.6 Reference Values

Per Section 3.5.6, the same principle is applied here. The airflow inlet values are utilized as the reference values. A sanity check is that the density calculated by Fluent is the same as the density included in Table 5.1.

5.5.7 Control and Monitor Settings

Under the Control tab, Fluent has options for the Courant Number, which has a default value of 1. The Courant number allows the solver to determine how far information travels across a cell in one time step. In other words, it controls numerical stability and accuracy. This project considers supersonic turbulent flow with ignition, further adding to the complexity that the solver has to consider. In conjunction with the size of the time steps, having a lower Courant number ensures that the information is not jumping multiple cells and therefore decreases the likelihood of numerical instability. For this project, it was lowered to the value of 1. The control tab also has the Under-Relaxation Factors: Turbulent Kinetic Energy, Turbulent Dissipation Rate, Turbulent Viscosity, and Solid. The under-relaxation factors quantify how the parameters, like velocity, pressure, temperature, etc, are updated per each interaction and utilizes the values imputed to dampen any significant changes. The default values are 0.8, 0.8, 1, and 1. As mentioned before, to account for the complex flow, the factors can be lowered to ensure stability. A consequence of this, however, is increasing the computational time. The values for this project are inputted to be 0.5, 0.5, 0.5, and 1.

As Section 3.2.7, the same convergence criteria value is considered.

5.5.8 Initialization

Standard initialization is selected. The inlet is selected for the area to compute the initialization from.

5.5.9 Running Calculation

It is in the Run Calculation tab, where a time step and number of time steps has to be declared as a result of running a transient simulation. To determine the time step to use, the following equation is considered:

$$\Delta t = \frac{CFL \cdot \Delta x}{V_{air}} \tag{39}$$

where CFL is the Courant number, Δx is the smallest cell size in the mesh, and V is the velocity of the airflow inlet. For a CFL value of 1, a Δx value of 1e-04, and the airflow inlet velocity calculated in Section 5.4.4, the time step value is approximately 8e-08 seconds.

The next step is to determine the number of time steps that should be examined. To begin, the time estimated for convergence is calculated using the following:

$$t_{conv} = \frac{length\ of\ combustor}{avg\ velocity\ in\ domain} \tag{40}$$

where the length of the combustion chamber is approximately 0.5 meters and the average velocity in the domain is estimated to be 2500 meters per second. This results in 0.2 milliseconds. To account for any instability to grow and then settle, the convergence time is multiplied by a factor of magnitude. The final result is 2 milliseconds, which is what is assumed will be the total simulation time for the flame to stabilize. Then, the following equation is used:

$$N_{steps} = \frac{t_{sim}}{\Delta t} \tag{41}$$

Substituting the values calculated above, the estimated number of time steps is 25,000.

These values can be inputted, and the default value for max iterations per time step can remain as is. The simulation can now be calculated.

6. Preliminary Results

Two CFD simulations were run, each having 1,000 time steps and each time step being the value calculated above. The results are found below.

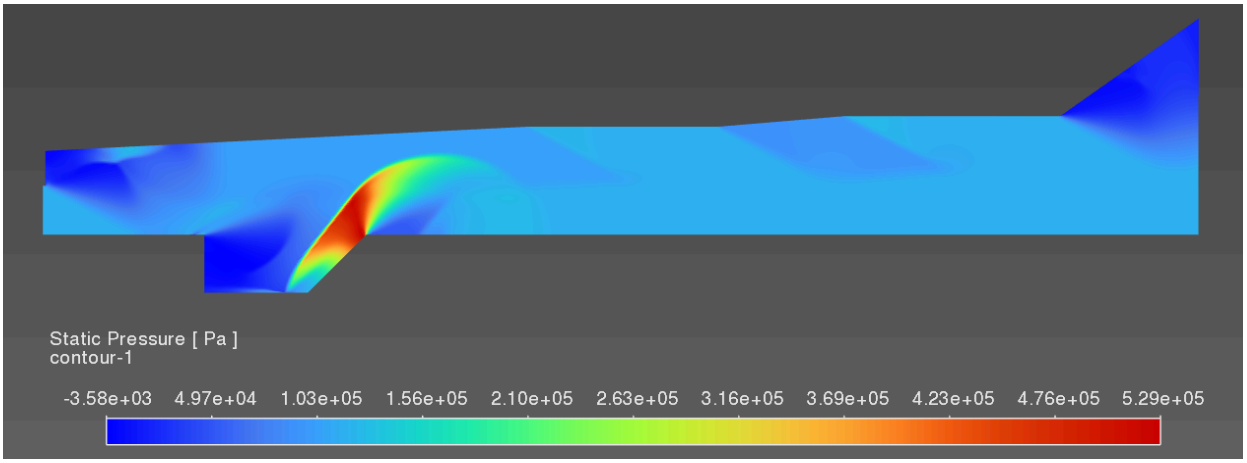

(a) 50 microseconds

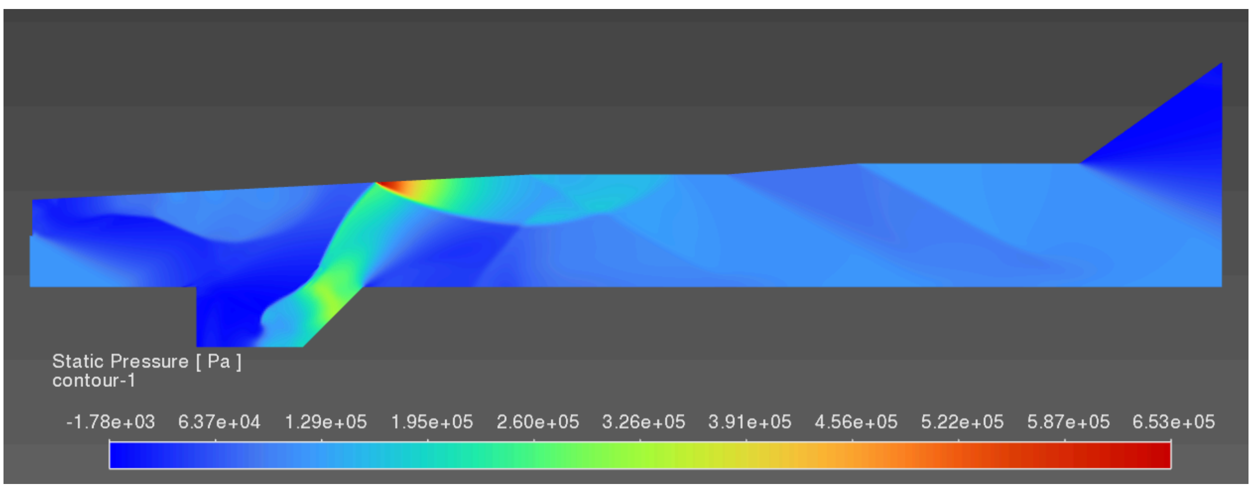

(b) 100 microseconds

Figure 6.1 - Static pressure contour as a result of fuel injection

For the current stage of the simulations, only the second fuel injector located above the airflow combustor inlet is active. From **Figure 6.1(a)**, there is a large high pressure region of approximately 530,000 Pa that follows the cavity, representing bow-shock interaction. At the end of 100 microseconds, **Figure 6.1(b)** demonstrates that the bow-shock interaction has begun to travel downstream, creating a smaller, more concentrated higher pressure region of approximately 650,000 Pa at the top of the combustor wall. Between **Figure 6.1(a)** and **Figure 6.1(b)**, the oblique shock wave train becomes more defined, although the pressure decreases as the flow travels downward.

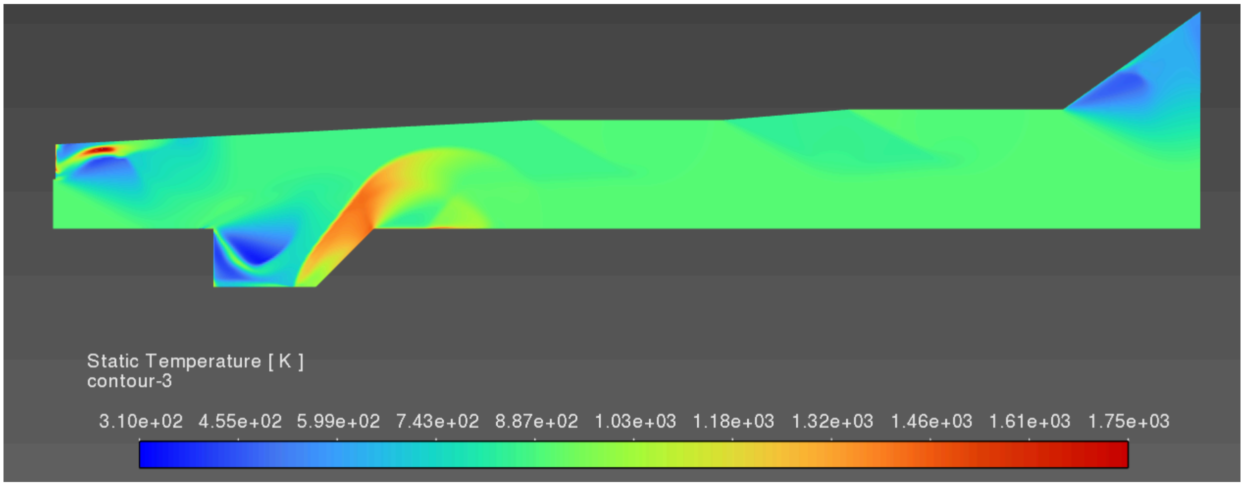

(a) 50 microseconds

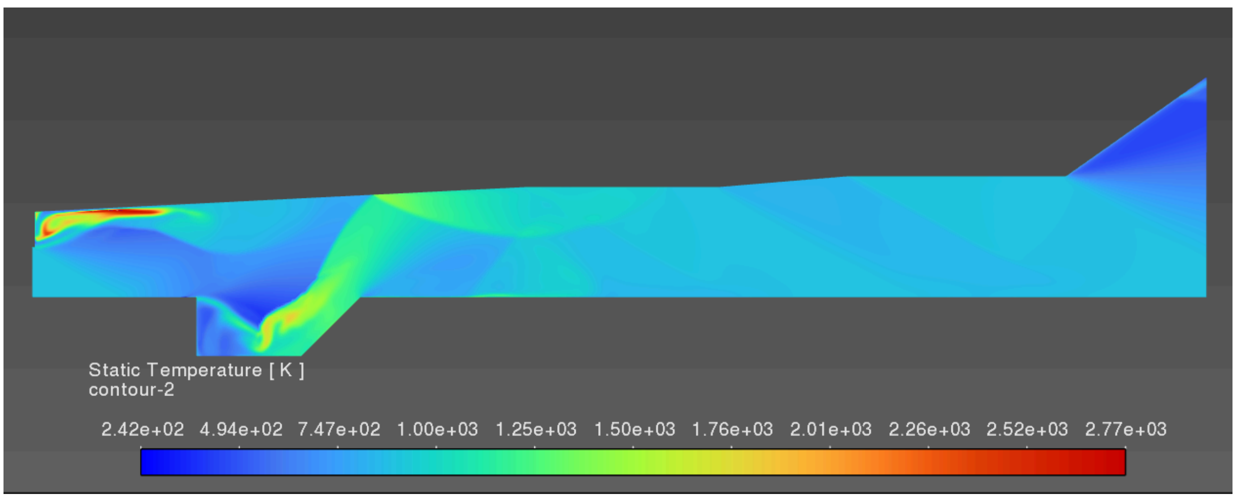

(b) 100 microseconds

Figure 6.2 - Static temperature contour after fuel injection

Exhibiting a similar pattern with the formation of a bow-shock structure and then the bow-shock beginning to travel downstream as the pressure contours, **Figure 6.2(a)** and **Figure 6.2(b)** further emphasize the effect the fuel being injected has on the incoming flow. Between the 50 microseconds and 100 microseconds, the upper wall experiences a small region of strong heating as a result of the burner inlet compression and the interaction between wall injector and the incoming boundary later. Downstream, there is a cooler region in the cavity, as seen in **Figure 6.2(a)**, that is a result of the relatively cold hydrogen jet penetrating the hotter air flow. Also downstream of the combustion chamber, the temperature distribution is once again dominated by compression heating due to the presence of the cavity.

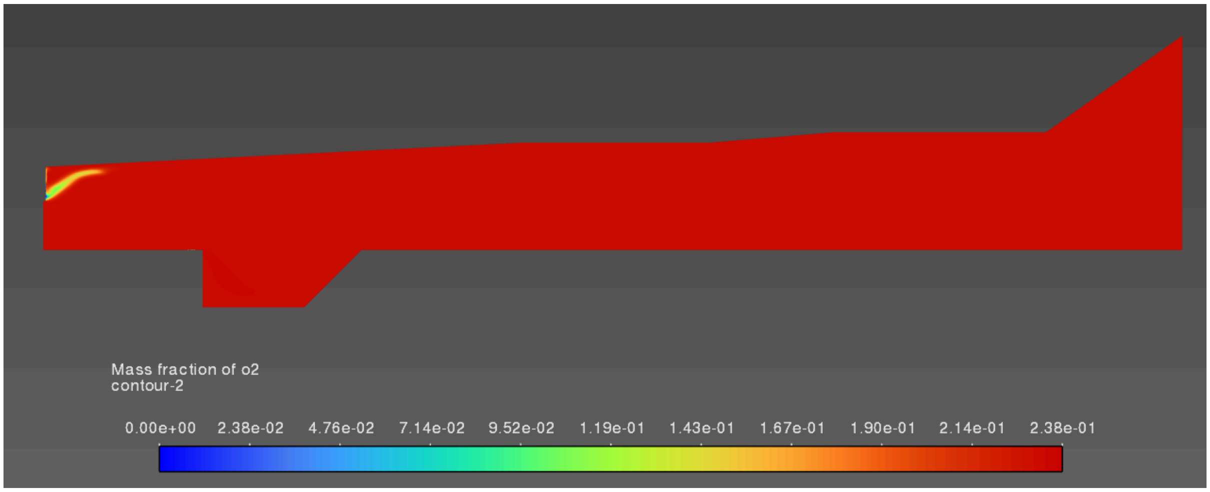

(b) 50 microseconds

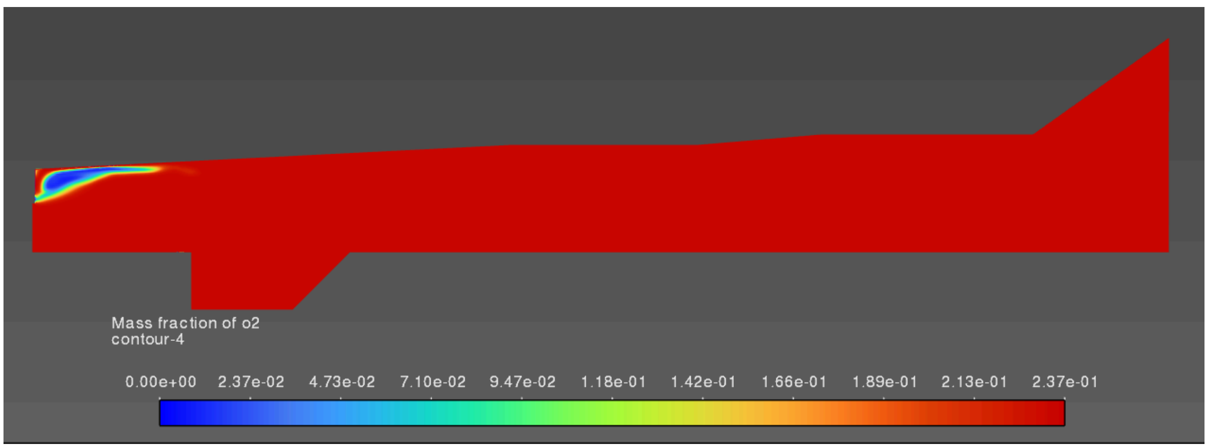

(b) 100 microseconds

Figure 6.3 - Mass fraction of oxygen after fuel injection

Figure 6.3(a) and **Figure 6.3(b)** further support what is known about the incoming flow, which is that it is approximately 24% oxygen. However, as the time increases, in the location of the second fuel injection, the mass fraction of oxygen decreases as it is being mixed with the liquid hydrogen.

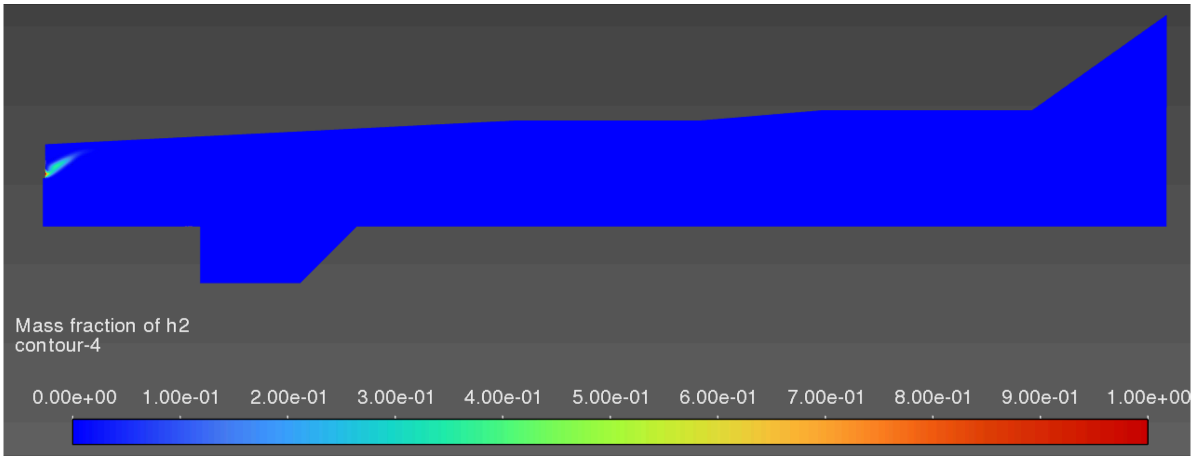

(c) 50 microseconds

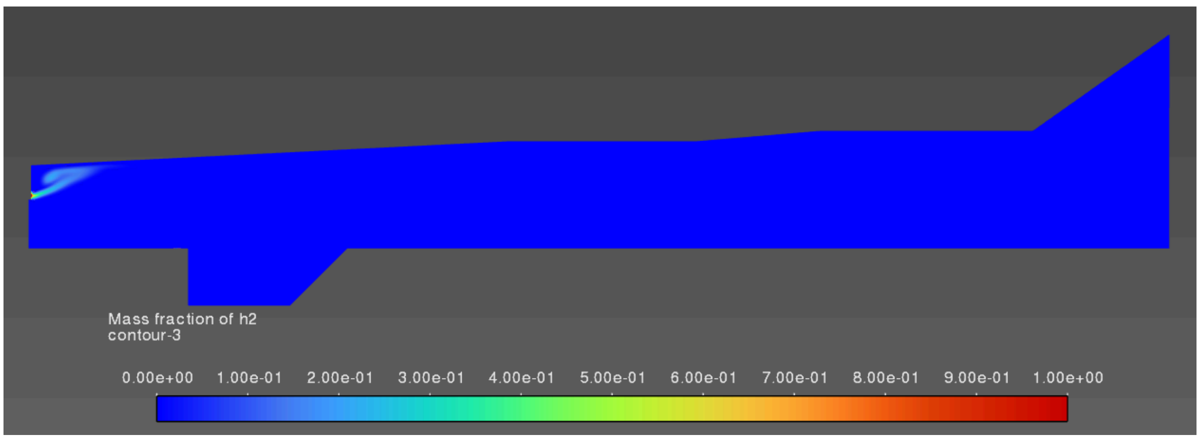

(b) 100 microseconds

Figure 6.4 - Mass fraction of liquid hydrogen after fuel injection

Figure 6.4(a) and **Figure 6.4(b)** further support that there should be no liquid hydrogen anywhere, except the location of the fuel injector. As time increases, it is seen that the fuel jet is expanding. Interestingly, there should be two active fuel injectors. Therefore, two hydrogen fuel jets should be seen in both figures. Not all of the hydrogen has been injected into the flow.

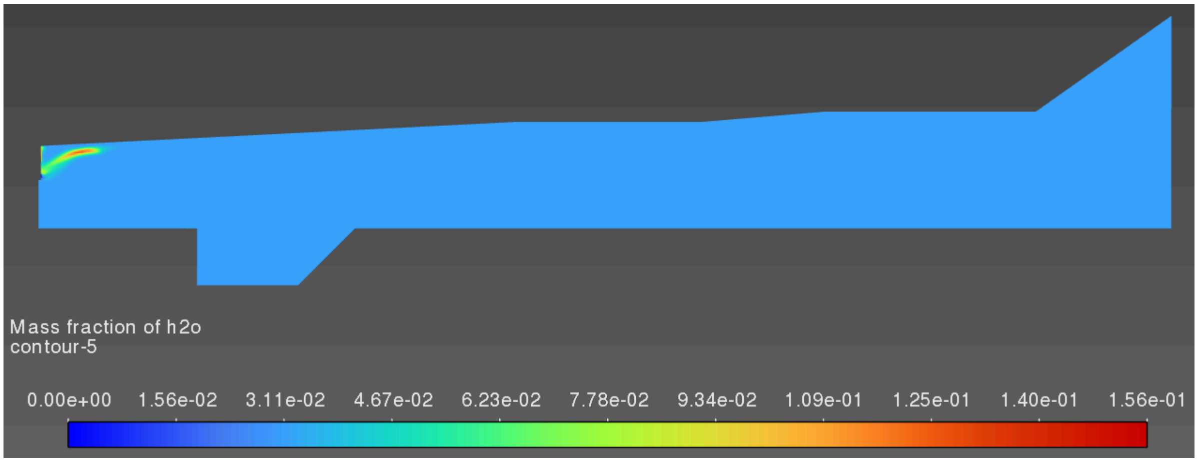

(d) 50 microseconds

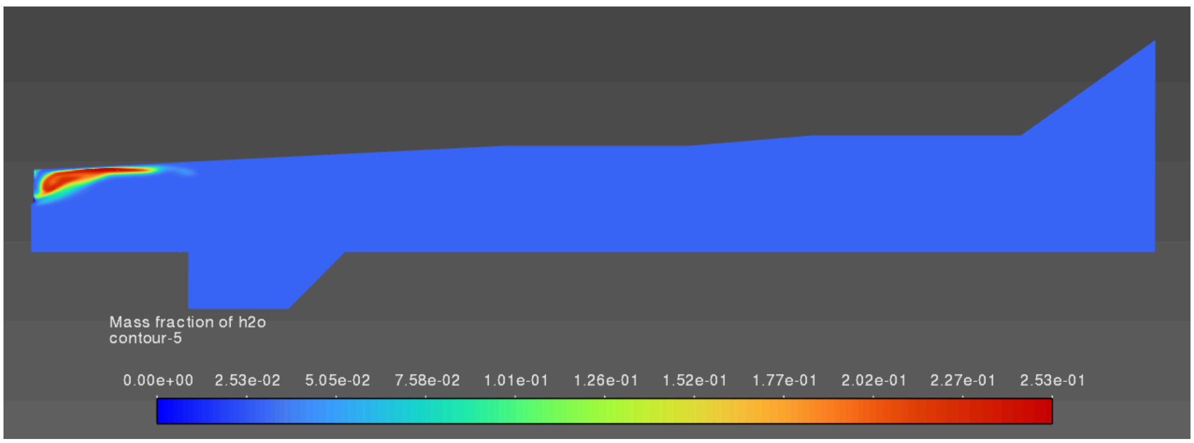

(b) 100 microseconds

Figure 6.5 - Mass fraction of water vapor after fuel injection

When oxygen and liquid hydrogen react, the result is water vapor. Thus, if the fuel and air did mix, there should be regions of water vapor near the injector. **Figure 6.5(a)** and **Figure 6.5(b)** support what is expected. It also emphasizes that the reaction carries downstream as time increases, which suggests that a flame is being developed.

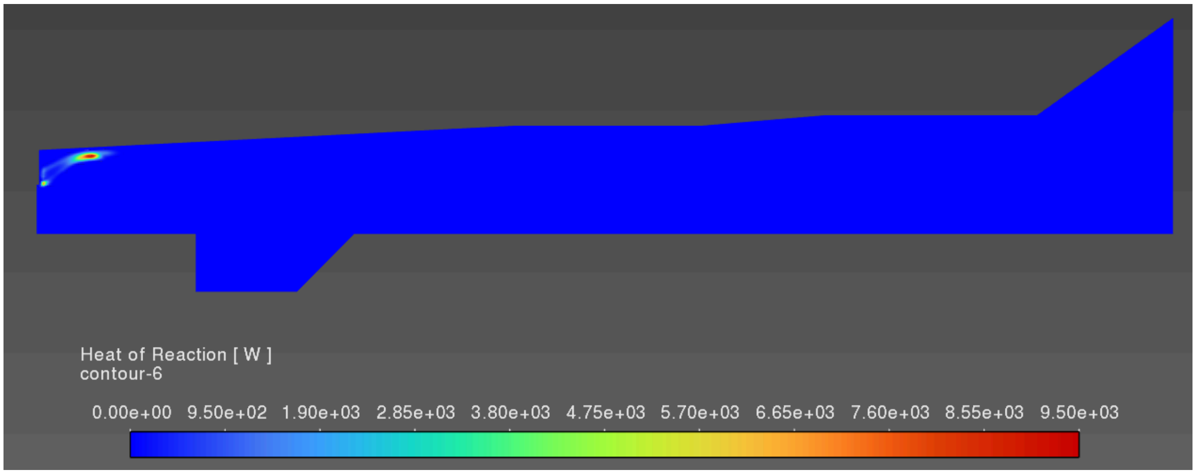

(a) 50 microseconds

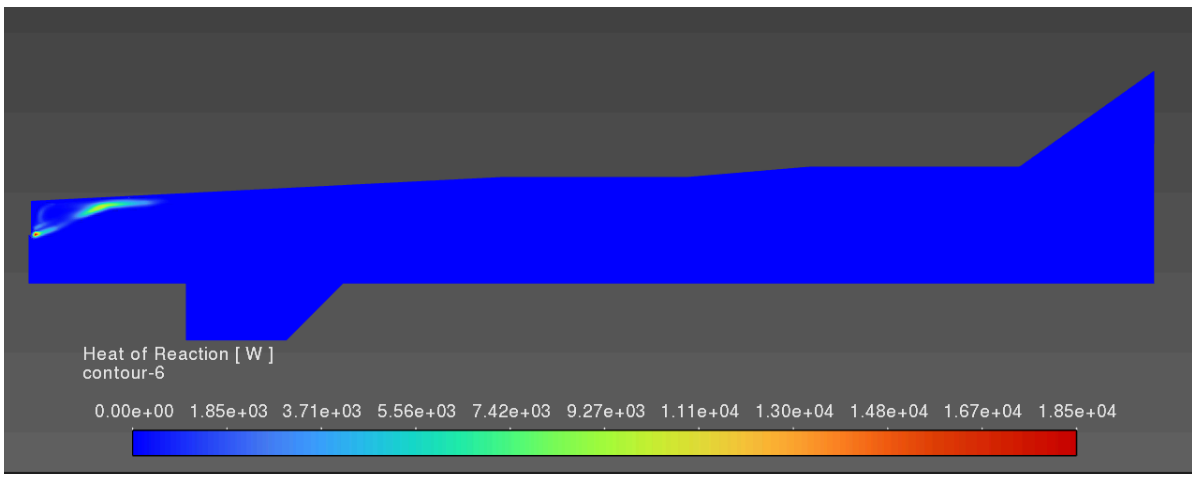

(b) 100 microseconds

Figure 6.6 - Heat of reaction after fuel injection

To further confirm that the reaction between air and the liquid hydrogen was occurring, the heat of reaction at 50 and 100 microseconds were produced, as seen in **Figure 6.6(a)** and **Figure 6.6(b)**, respectively. In the time span, the reaction grows in domain and in magnitude. Initially, the reaction was releasing energy on the order of 10^3. However after 100 microseconds, the heat releases increases to the order of 10^4. This demonstrates that the reactions are occurring as originally intended, and a flame is beginning to develop. Both **Figure 6.6(a)** and **Figure 6.6(b)** display that the rest of the domain is cold, non-reacting as the heat of reaction is zero.

7. Conclusion and Future Work

In recent years, there has been a renewed interest in hypersonic flight, which results in the continuing development of air-breathing propulsion systems that are capable of operating at the required supersonic speeds. Among those air-breathing propulsion systems, the supersonic combustion ramjet is of particular interest to engineers as it offers the potential for efficient propulsion in the hypersonic regime, in theory. However, scramjet combustors are difficult to design and operate. Ignition and maintaining a stable flame must occur within short residence times. It is also difficult to maintain a highly compressible flow environment, further emphasizing how every detail of the scramjet must be carefully considered.

In theory, physical experiments are the first step to obtain real-world accuracy and attempt to capture varying parameters. In the case of scramjets, it is difficult to conduct such experiments, such as wind tunnel tests, due to the limitations on replicating the supersonic turbulent air at high altitudes while being affordable. This illustrates the need for numerical analysis, as it offers more options in creating an extremely similar environment that the scramjet needs.

From a physical-modeling perspective for numerical analysis, the reaction mechanism is the first fundamental lever that influences the predicted ignition, flame stabilization, and heat release in a scramjet combustion chamber. However, these combustion processes are also strongly coupled with the surrounding flow field. The presence of thick shear layers, interconnected shocks, shear-layer/shock interactions, and turbulent mixing must also be considered. The combined influence of the coupled phenomena implies that ignition, flame anchoring, and heat release are controlled by plenty of interacting parameters. As a result, it is inherently difficult to obtain quantitatively accurate predictions of scramjet combustion. A requirement to do so is considering treatment of both the reaction mechanism and flow features that govern any mixing and local thermochemical conditions.

While there are plenty of scramjet designs available in literature, the configuration utilized in this project was the CIAM/NASA scramjet, which was constructed in Solidworks. It is one of the few scramjet designs that includes all the components, the inlet, isolator, combustion chamber, and nozzle. In addition, the scramjet was one of the first to have flight data validated with ground tests, achieving Mach 6.4 at approximately 22 kilometers. For this project, it was deemed that analyzing the entirety of the scramjet, rather than the components individually, would be more beneficial. The analysis of the coupled flow and combustion physics would be analyzed in a setting that closely resembles an operating scramjet, in general, which provides a more realistic basis.

To reiterate, the main learning objective for this project centered on developing a better understanding of the effect the number of reaction mechanisms considered, when injecting liquid hydrogen into supersonic turbulent air at a high altitude, has on the overall combustion efficiency of the CIAM/NASA scramjet. Furthermore, the objective can provide guidelines for mechanism selection for future scramjet design and analysis. The theoretical framework required for the analysis was Reynolds-Averaged-Navier-Stokes Equations, which include continuity, momentum, and energy affected by turbulent flow.

Minor geometry modifications were done on the computer-aided design software ANSYS Spaceclaim. The meshing was accomplished using ANSYS Mechanical as the final mesh is directly uploaded to ANSYS Fluent. To run the computational fluid dynamic simulations accurately, assumptions were made about the geometry and the boundary conditions. While there is literature regarding the major specifications of the CIAM/NASA scramjet, there were intricate details on the scramjet that did not have any measurements. These measurements were inferred by the surrounding geometry. When considering the fuel injectors, parameters were found solely for the combustion chamber, resulting in a change in the original geometry. The fuel injectors themselves, which are cylindrical in nature and aligned in a cylindrical coordinate system, were assumed to be slits in their respective locations and the burner was assumed to be rectangular. Regarding the boundary conditions, the same literature sources mentioned parameters such as total temperature, Mach number, and density. Assuming an ideal gas for the airflow entering the scramjet, and therefore using ideal gas relations, static temperature and pressure were calculated.

Solver settings were set to account for the turbulent, compressible flow, shock-waves, and shear layers. To ensure accuracy in the design, a validation simulation was conducted, neglecting fuel injection, using the SST k-ω turbulence model, and considering steady flow. The results were compared to literature as well as oblique shock wave theory. To correctly compare the CFD simulation results, the inlet was defined two ways. For comparison to oblique shock wave theory, the inlet was defined as beginning immediately after the third oblique shock wave, which places it before the cowl tip. For comparison to literature, the inlet was defined by where it ends, i.e. where the isolator begins. Both comparisons found that the CFD simulation results were within range, implying that the simulation set up was done correctly and the physics is being replicated correctly.

For fuel injection integration, most of the CFD solver settings from the validation run were applied, the turbulence model was modified to realizable k-ε, the flow was considered transient, and the fuel-air mixture reaction rates were finite-rate/eddy-dissipation with the default reaction mechanism of four reactions. Despite providing Fluent with the injector exit conditions for both the second and third injector, and ensuring both were set to inlet types, it was found that only the second injector was active during the simulation representing 100 microseconds of the combustion time. While this does reduce the complexity of the flow field, the goal is to set up the simulation to what has already been done. Regardless, the simulation does demonstrate that for the second fuel injector, fuel was injected into the flow as the mass fraction of oxygen decreases near the injector, the mass fraction for liquid hydrogen increases, and the mass fraction of water vapor also increases. These trends indicate that there is fuel-air mixing and that the flame is beginning to develop. The pressure and temperature distribution demonstrate that there is a bow-shock interaction that creates concentrated regions of higher pressure and higher temperature, which will be helpful for the fuel-air mixing when it comes for the flame to reach that section of the combustion chamber.

In the attempt to model the CIAM/NASA scramjet combustion chamber as realistically as possible, several key limitations were encountered. The major limitation of the present work is that the thesis main learning objective, of comparing the combustion efficiency of different reaction mechanisms, was not fully achieved. The combination of a detailed chemistry, high Mach number resulting in extreme boundary conditions, and intense interactions between the shear layers at the walls and the flame led to restrictive time-step requirements in the transient solve for numerical stability. In turn, this results in long simulation times for the number of time steps required to reach a flame stabilization. It was found that the length of the simulation, when the number of time steps considered is more than a couple thousand, amounts to days. Moreover the software crashes as a result of computer hardware limits. Consequently, the results account for a short physical time and should be primarily interpreted as ignition tendency, flame development, and species trend, rather than full ignition, flame stabilization, and complete reaction heat release. The computational power available also put a restriction on the element size chosen for the mesh of both the entire CIAM/NASA scramjet and its combustion chamber only.

Although archival literature on the CIAM/NASA scramjet provided enough information to reconstruct the overall geometry and nominal operating conditions, the available data was sufficient to establish a basic set of boundary conditions for the simulations. Many important details, such as exact inlet profiles, turbulence quantities, predicted fuel injector conditions for all three fuel injector stations, were not fully specified in open literature. As a result, several modelling choices had to be based on reasonable assumptions or on values inferred from related studies. These assumptions introduce additional uncertainty into the simulations and may contribute to discrepancies in the quantitative prediction of ignition behavior, flame location, and overall combustor performance.

A further limitation concerns the choice of turbulence model for the reacting fuel-injection simulations. Although the SST k-ω turbulence model would, in principle, be better suited to capturing shock-boundary layer interactions and near-wall phenomena in the scramjet combustor, repeated attempts to use SST k-ω in combination with detailed chemistry led to severe numerical divergence. This behavior is likely linked to the sensitivity of the SST model to near-wall resolution and to the presence of strong, steep gradients in the injection region, in combination with a mesh that could not be refined arbitrarily due to computational constraints. Consequently, the k-ε model had to be used instead. While this choice improved robustness and allowed the simulations to run, it may limit the accuracy of the predicted boundary layer development and shear-shear layer interactions. Thus, it introduces additional uncertainty into the detailed structure of the reacting flow.

Another limitation of the study is the use of two-dimensional representation of the combustor geometry. It should also be noted that, although the non-reacting validation case was modelled as axisymmetric to better reflect the nominally annular scramjet geometry, the reacting fuel injection cases were restricted to a two-dimensional planar domain. This simplification was necessary to keep the computational cost manageable when detailed chemistry and very small time steps were required. As a consequence, the results for the reacting case should be interpreted as representative of a planar slice of the combustor rather than a fully three-dimensional description of the flow and flame structure.

The more feasible constraint that should be addressed first is mesh refinement near the injector regions, shear layers, and near-wall zones to enable robust use of the SST k-ω turbulence model for the reacting fuel injection case. A systematically refined grid, combined with careful control of under-relaxation factors and time-step size, would allow the SST k-ω turbulence model to be used as originally intended, improving the representation of shock-boundary later interaction and near-wall turbulence. This would thereby reduce one important source of modelling uncertainty.

Another direction would be to complete the original main learning objective of this thesis by considering the number of time steps required to visualize flame stabilization. The current work done is restricted to relatively short time scales that primarily capture ignition onset, and the beginning of flame development. As mentioned before the inlet burner boundary conditions were extrapolated from CIAM/NASA scramjet flight test data and one-dimensional analysis. As initially intended, the entirety of the scramjet was meant to be analyzed. A potential extension would be to calculate the fuel injection conditions for all three fuel injector stations based on the freestream conditions, as well as results presented from cold flow CFD simulations. This could allow for a comparison between the entire scramjet and just the combustion chamber to further explore key parameters such as flame stabilization and heat release.

Finally, future studies could benefit from exploring alternative CFD solvers that are specifically optimized for stiff reacting flows and detailed chemistry. This masters project was constrained by the computational cost and stability limits of the chosen solver when small time steps were employed. A software with more advanced implicit time-integration schemes, tailored preconditioners, or dedicated combustion modules may allow detailed hydrogen-air mechanisms to be advanced over longer physical times at an acceptable and reliable cost. Cross-comparing results from different solvers for the same geometry and boundary conditions would also provide valuable measure of numerical robustness and assist in distinguishing physical trends from solver-dependent settings. Taken together, these extensions have the potential of transforming this study from an initial exploration of detailed chemistry in a scramjet combustion chamber into a robust predictive framework that can meaningfully inform the design and assessment of future hypersonic propulsion systems.

References

[1] Northrop Grumman, "Next-Generation Scramjet Delivers Hypersonic Propulsion That Weighs Less to Pack More Punch," Northrop Grumman, accessed 20 February 2025. https://www.northropgrumman.com/what-we-do/advanced-weapons/northrop-grummans-next-generation-scramjet

[2] Hermeus, "Halcyon," Hermeus, retrieved 15 February 2025. https://www.hermeus.com/halcyon

[3] NASA, "X-43A Hyper-X," NASA, retrieved 15 February 2025. https://www.nasa.gov/reference/x-43a/

[4] Smart, M. K., "Scramjet Inlets," NATO, 2010.

[5] "Ramjet propulsion," *NASA* Available: https://www.grc.nasa.gov/www/k-12/airplane/ramjet.html.

[6] Ma, G., Zhao, G., Sun, M., Xiong, D., Li, F., Liu, M., and Wang, H., "On compression level of hypersonic airflow in high-mach scramjet," *Energy*, Vol. 295, 2024. https://doi.org/10.1016/j.energy.2024.130993

[7] Choubey, G. and Tiwari, M., "Introduction," *Scramjet Combustion: Fundamentals and Advances*, Elsevier, Cambridge, MA, 2022, pp. 1-17.

[8] Andreadis, D., "Scramjet engines enabling the seamless integration of air & space operations," *Pratt & Whitney Space Propulsion,* Hypersonics, West Palm Beach, Fl, 2004.

[9] Drummond, J. P., Diskin, G. S., and Cutler A. D., "Chapter 6: Fuel-Air Mixing and Combustion in Scramjets," NASA 20060020221, January 2006.

[10] Shen, W., Huang, Y., Liu, Z., and You, Y., "Mixing and transient combustion processes of scramjet combustor with transverse injector and hypermixer," *Case Studies in Thermal Engineering*, Vol. 26, 2021. https://doi.org/10.1016/j.csite.2021.101104

[11] NASA, "Brayton Cycle," NASA, retrieved 15 February 2025. https://www.grc.nasa.gov/www/k-12/airplane/braytonram.html

[12] Segal, C., *The Scramjet Engine: Processes and Characteristics*, Cambridge University Press, 2009

[13] Segal, C., "Propulsion Systems for Hypersonic Flight," NATO, 2024.

[14] Roddy, M., "Combined Cycles for Reusable and CostEfficient Space Flight." AIAA Session: Freshman & Sophomore Open Topic Category, 2024. https://doi.org/10.2514/6.2023-70864

[15] Roberts, K. N., "Analysis and Design of a Hypersonic Scramjet Engine with a Starting Mach Number of 4.00," Master's Thesis, Aerospace Engineering Dept., Univ. of Texas at Arlington, Arlington, Texas, 2008.

[16] Fry, R. S., "A Century of Ramjet Propulsion Technology Evolution," *Journal of Propulsion and Power*, Vol. 20, No. 1, 2004. https://doi.org/10.2514/1.9178

[17] Distaso, E., Cassone, E., Tamburrano, P., Amirante, R., and De Palma, P., " Characterization of the hydrogen combustion process in a scramjet engine," International Journal of Hydrogen Energy, Vol. 71, 2024, pp. 650-661. https://doi.org/10.1016/j.ijhydene.2024.05.184

[18] Engman, E., "Numerical Simulation of Scramjet Combustion," Master's Thesis, Dept. of Applied Physics and Mechanical Engineering, Luleå Univ. of Tech., Sweden, 2008.

[19] Tian, Y., Shi, W., Guo, M., Liu, Y., Zhang, C., and Le, J., "Investigation of combustion characteristics in a hydrogen-fueled scramjet combustor," *Acta Astronautica*, Vol. 186, 2021, pp. 486-495. https://doi.org/10.1016/j.actaastro.2021.06.021

[20] Ma, K., Zhanga, Z., Liu, Y., and Jiang, Z., " Aerodynamic principles of shock-induced combustion ramjet engines," *Aerospace Science and Technology*, Vol. 104, 2020. https://doi.org/10.1016/j.ast.2020.105901

[21] Deng, J., Guo, M., Chen, E., Tian, Y., Chunmei, C., and Zhang, H., " Evolution prediction of flame structure in a hydrogen-fueled scramjet combustor based on lightweight deformable convolutional residual neural network," *Engineering Applications of Artificial Intelligence*, Vol. 138, 2024. https://doi.org/10.1016/j.engappai.2024.109435

[22] Madhumitha, R. and Karmakar, S., "Boron-loaded gel fuel as potential fuel for ramjet and scramjet engines- recent advancements," *FirePhysChem*, Vol. 4, 2024, pp. 185-200. https://doi.org/10.1016/j.fpc.2023.07.003

[23] Sam, L., Idithsaj, P. T., Nair, P. P., Suryan, A., and Narayanan, V., "Prospects for scramjet engines in reusable launch applications: A review," International Journal of Hydrogen Energy, Vol. 28, Is. 92, 2023, pp. 36094-36111. https://doi.org/10.1016/j.ijhydene.2023.05.341

[24] Smart, M. K., "Scramjets," NATO RTO-EN-AVT-150 , 2007.

[25] Philippou, A. L., Zachos, P. K., & MacManus, D. G."Aerodynamic Instabilities in High-Speed Air Intakes and Their Role in Propulsion System Integration," *Aerospace*, Vol. 11, 2024. https://doi.org/10.3390/aerospace11010075

[26] Siddiqui, A. M., and Ahmed, G. M. S., "Design and Analysis on Scramjet Engine Inlet," *International Journal of Scientific and Research Publications*, Vol. 3, 2013. http://www.ijsrp.org/research-paper-1301.php?rp=P13590

[27] Alhassani, A. K., Mohamed, M. T., Fares, M., and Dol, S. S., "Shock waves analysis of the novel intake design system for a scramjet propulsion," *Wseas Transactions on Systems*, Vol. 20, 2021. DOI:10.37394/23202.2021.20.9

[28] Anderson, J. D., *Fundamentals of aerodynamics*, New York, New York: Mcgraw-Hill, 2011.

[29] Araújo, P. P. B., Pereira, M. V. S., Marinho, G. S., Martos, J. F. A., & Toro, P. G. P., "Optimization of scramjet inlet based on temperature and Mach number of supersonic combustion," *Aerospace Science and Technology*, Vol. 116, 2021. https://doi.org/10.1016/j.ast.2021.106864

[30] Smart, M. K., "Scramjet Isolator," NATO RTO-EN-AVT-185, 2010

[31] Chengpeng, W., Longsheng, X., Xuang, T., "Experimental characteristics of oblique shock train upstream propagation," *Chinese Journal of Aeronautics*, Vol. 30, Is. 2, 2017, pp. 663-676. https://doi.org/10.1016/j.cja.2017.02.004

[32] Musielak, D., *Scramjet Propulsion: A Practical Introduction,* Wiley, 2023

[33] Selezneva, R.K., Surzhikova, S.T., Shang, J.S., "A review of the scramjet experimental data base," *Progress in Aerospace Sciences*, Vol. 106, 2019, pp. 43-70. https://doi.org/10.1016/j.paerosci.2019.02.001

[34] McClinton, C., Roudakov, A., Semenov, V., Kopehenov, V., "Comparative flow path analysis and design assessment of an axisymmetric hydrogen fueled scramjet flight test engine at a Mach number of 6.5," *Space Plane and Hypersonic Systems and Technology Conference*, AIAA, 1996. https://doi.org/10.2514/6.1996-4571

[35] Voland, R., Auslender, A., Smart, M., Roudakov, A., Semenov, V., Kopchenov, V., "CIAM/NASA Mach 6.5 scramjet flight and ground test," *9th International Space Planes and Hypersonic Systems and Technologies Conference*, AIAA, 1999. https://doi.org/10.2514/6.1999-4848

[36] Roudakov, A., Semenov, V., Kopchenov, V., Hicks, J., "Future flight test plans of an axisymmetric hydrogen-fueled scramjet engine on the Hypersonic Flying Laboratory," *Space Plane and Hypersonic Systems and Technology Conference*, AIAA, 1996. https://doi.org/10.2514/6.1996-4572

[37] The Engineering ToolBox, "U.S. Standard Atmosphere vs. Altitude," retrieved 28 April 2025. https://www.engineeringtoolbox.com/standard-atmosphere-d_604.html

[38] NASA, "Navier-Stokes Equations," accessed 3 October 2025. https://www.grc.nasa.gov/www/k-12/airplane/nseqs.html

[39] Anderson, J. D., *Computational Fluid Dynamics: The Basics with Application*, New York, New York: Mcgraw-Hill, 1995.

[40] ANSYS, "5.2.1 Heat Transfer Theory," retrieved 3 October 2025. https://www.afs.enea.it/project/neptunius/docs/fluent/html/th/node107.htm

[41] ANSYS: Part of Synopsys, "What is Turbulent Flow?," retrieved 3 October 2025. https://www.ansys.com/simulation-topics/what-is-turbulent-flow

[42] Massachusetts Institute of Technology News, "Understanding how fluids heat or cool surfaces," retrieved 3 October 2025.
https://news.mit.edu/2020/how-fluids-heat-cool-surfaces-0428

[43] Embry Riddle Aeronautical University, "Turbulent Flows," retrieved 3 October 2025.https://eaglepubs.erau.edu/introductiontoaerospaceflightvehicles/chapter/turbulent-flows/

[44] ANSYS, "Standard and SST k-ω Models," retrieved 3 October 2025.
https://www.afs.enea.it/project/neptunius/docs/fluent/html/th/node65.htm

[45] Rodriguez, C.G., "CFD Analysis of the CIAM/NASA Scramjet," *38th Joint Propulsion Conference & Exhibit*, AIAA, 2003. https://doi.org/10.2514/6.2002-4128